# Quantum printing and induced vorticity in superconductors II: Laguerre-Gaussian beam

Tien-Tien Yeh,[1,2,*] Hennadii Yerzhakov,[2] Logan Bishop-Van Horn,[3] Srinivas Raghu,[3] and Alexander Balatsky[1,2,†]
[1]*Department of Physics, University of Connecticut, Storrs, Connecticut 06269, USA*
[2]*Nordita, Stockholm University, and KTH Royal Institute of Technology, Hannes Alfvéns väg 12, SE-106 91 Stockholm, Sweden*
[3]*Department of Physics, Stanford University, Stanford, California, USA*

(Received 16 December 2024; accepted 7 September 2025; published 28 October 2025)

The challenge of controlling the quantum states of matter via light has been at the forefront of modern research on driven quantum matter. We explore the imprinting effects of structured light on superconductors, demonstrating how the quantum numbers of light—specifically spin angular momentum, orbital angular momentum, and radial order—can be transferred to the superconducting (SC) order parameter and control vortex dynamics. Using Laguerre-Gaussian beams, we show that by tuning the quantum numbers and the amplitude of the electric field, it is possible to manipulate a variety of vortex dynamics, including breathing vortex pairs, braiding vortex pairs, vortex droplets, and swirling two-dimensional vortex rings. More complex structures of vortex clusters, such as vortex flake structures, and standing wave motions, also emerge under specific quantum numbers. These results demonstrate the ability to control SC vortex motion and phase structures through structured light, offering potential applications in quantum fluids and optical control of superconducting states. Our findings present a diagram that links light's quantum numbers to the resulting SC vortex dynamics, highlighting the capacity of light to transfer its symmetry onto superconducting condensates. We point out that this approach represents the extension of printing to quantum printing by light in a coherent state of electrons.

DOI: 10.1103/dqv7-w2w4

## I. INTRODUCTION

Optical printing has evolved significantly over the past few decades. Beyond everyday applications, advanced methods such as laser printing on different materials, including bubbles and plasmonic nanoparticles [1,2], optical coloration, decolorization, or erasable printing [3–6], volumetric printing [7,8], and holographic printing [9] have been reported.

Structured light tailored with quantum numbers (QNs) enables the direct printing of these QNs onto the condensed electron liquids, offering precise control over matter states and inducing specific topological and dynamical responses within the material. In condensed matter physics, recent progress in optical control of materials now includes control of chiral phonon dynamics by spin angular momentum (SAM) coupling [10–12], orbital angular momentum (OAM) transfer to magnets [13], induction of skyrmions [14], induction of spiral Higgs waves [15], creation of polariton vortices [16,17], Kapitza engineering in superconducting (SC) devices [18], and even induction of chiral mass and charge of electrons [19]. These examples showcase the emerging potential of optical manipulation of electron behavior and superconducting state.

In superconductors, the coherent quantum electron liquid can be "stirred up" by the dynamical electromagnetic gauge potential, which allows for the transfer of the QNs of structured light to SC coherent states. In our previous work, "Quantum Printing and Induced Vorticity in Superconductors I: Linearly Polarized Light" [20], we theoretically demonstrated that linearly polarized light can imprint itself on SC fluid inducing transient vortex-antivortex pairs (VPs) due to oscillating magnetic flux provided by the nonhomogeneous Gaussian structured beam.

In this work, we extend the investigation to SC coherent states interacting with light carrying nonzero QNs, including SAM, OAM, and radial order (number of rings of electric field), as shown schematically in Fig. 1. These QN-carrying light sources are realized through Laguerre-Gaussian (LG) beams. We demonstrate how structured light carrying SAM and OAM induces rotating/revolving or braiding vortices. Unlike circularly polarized light, OAM introduces additional out-of-plane flux, resulting in unusual dynamics. Using a hydrodynamic approach to quantum fluid, we analyze these dynamically imprinted patterns, investigating the supercurrent and vortex responses to QN-carrying light. Our focus is on light sources within the $10^{-1}$ to $10^{1}$ THz range, where wavelengths are on the order of microns or larger. In this series of studies, we simulate the dynamics of the superconducting state in SC thin films subjected to incident QN-carrying light using the generalized time-dependent Ginzburg-Landau (gTDGL) model.

We view the presented approach of imprinting QNs of light onto coherent electron liquid as an example of *quantum printing* where the coherent fluid of electrons "senses"

*Contact author: ttyeh0212@gmail.com
†Contact author: balatsky@hotmail.com

*Published by the American Physical Society under the terms of the Creative Commons Attribution 4.0 International license. Further distribution of this work must maintain attribution to the author(s) and the published article's title, journal citation, and DOI. Funded by Bibsam.*

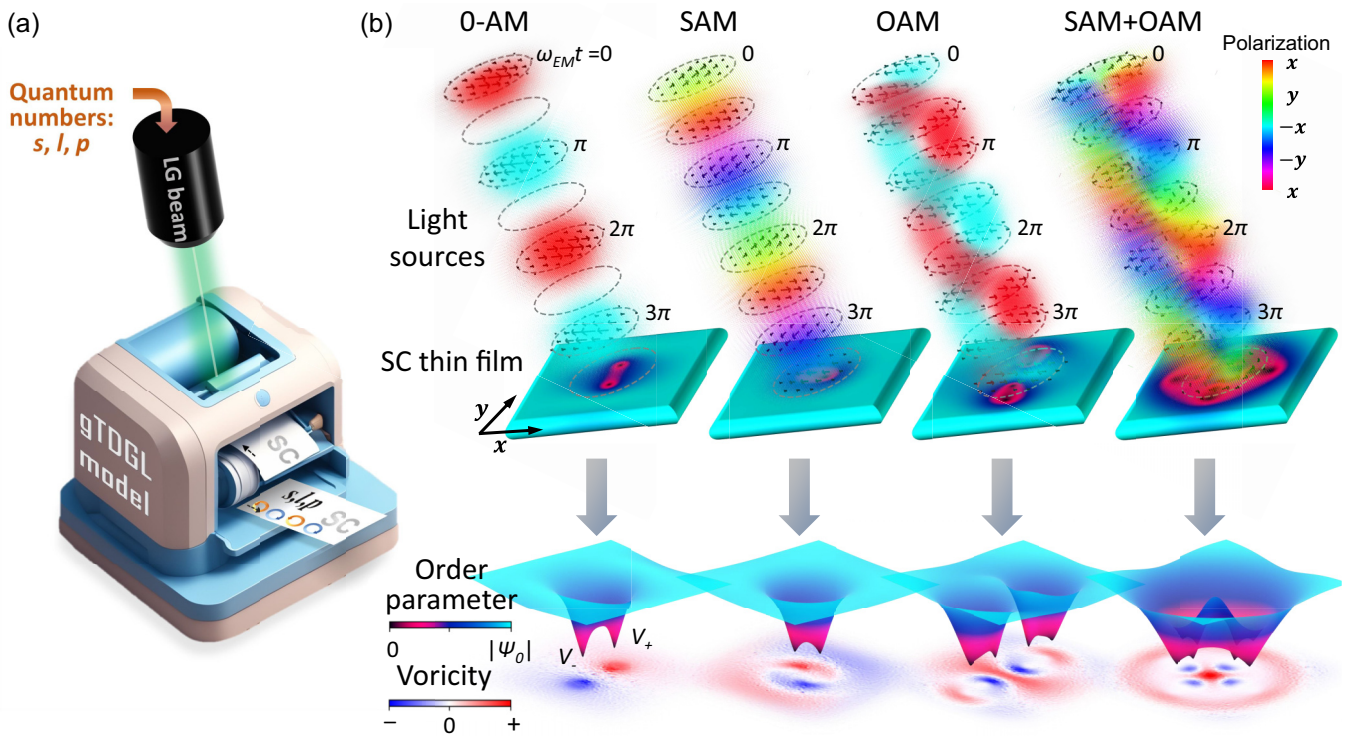



FIG. 1. (a) A toy model of quantum printing (Partially artificial intelligence-generated image [21]). Within the framework of the gTDGL model, the $s$, $l$, and $p$ present the quantum numbers corresponding to the SAM, OAM, and radial order of structured light, respectively. The input and output papers in the printer symbolize the SC thin film before and after imprinting of quantum numbers, respectively. (b) A schematic diagram illustrating the profile of the order parameter and vorticity of the current density induced by structured light. The light propagates normally onto SC thin film. The section of the SC thin film shows the time evolution of light source under different angular momentum (AM) configurations: 0-AM (no AM), SAM ($s = 1, l = 0$), OAM ($s = 0, l = 1$), and SAM + OAM (combining $s = 1$ and $l = 1$). The colored region represents the polarization as color bar, with the color intensity. The black dashed circle with arrows inside depicts snapshots of the electric field at different time, $\omega_{\mathrm{EM}}t$, where arrows indicate the field direction. The color on the SC surface represents the order parameter as a color map. The figures below the gray arrows show the order parameters affected by structured light and the corresponding vorticity of the supercurrent.

and responds to structured light in a systematic and coherent manner reflecting the possibility to manipulate coherent states with light.

This paper is organized as follows: We show the simulation method in Sec. II A, the light sources in Sec. II B, and the simulation conditions in Sec. II C. We show the resulting dynamics of SC states subjected to light with different SAM and OAM in Sec. III A and the influence of QNs that control the number of radial nodes of light or so-called radial order (RO) or radial index in Sec. III B. In Sec. III C, we conclude with the types of vortex dynamics induced by different QNs.

## II. METHOD: TIME-DEPENDENT GINZBURG-LANDAU THEORY

### A. Generalized time-dependent Ginzburg-Landau theory

We use the gTDGL model to explore supercurrent and vortex dynamics. The gTDGL model is described by the following equation in dimensionless units [22–24]:

$$\frac{u}{\sqrt{1+\gamma^2|\psi|^2}}\left(\frac{\partial}{\partial t}+i\mu+\frac{\gamma^2}{2}\frac{\partial|\psi|^2}{\partial t}\right)\psi = (1-|\psi|^2)\psi+(\nabla-i\boldsymbol{A})^2\psi. \quad (1)$$

Here, $\psi$ is the complex order parameter, i.e., $\psi = |\psi|\exp i\theta_s$. The term $(\frac{\partial}{\partial t}+i\mu)$ is the covariant time derivative with scalar potential $\mu$, and the term $(\nabla - i\boldsymbol{A})^2$ represents the covariant Laplacian with vector potential $\boldsymbol{A}$ from light sources, which will be discussed in the following section. The parameter $\gamma$ and the constant $u$ are determined by the influence of inelastic scattering processes and the ratio of the relaxation times of the order parameter and current, respectively. Further details regarding the equation including used dimensionless units are provided in Ref. [20]. The total current density is given by

$$\boldsymbol{J} = \boldsymbol{J}_s + \boldsymbol{J}_n = \mathrm{Im}[\psi^*(\nabla - i\boldsymbol{A})\psi] - \nabla\mu - \frac{\partial \boldsymbol{A}}{\partial t}, \quad (2)$$

where $J_s$ and $J_n$ denote the supercurrent density and normal current density, respectively.

The simulation is built upon a python-based script, a package LG-TDGL. Further details regarding the symbols and the gTDGL simulation can be found in the Supplemental Material [25,26].

### B. Light sources: LG beams

Structured light, such as LG beams, Hermite-Gaussian beams, and Bessel beams [27], offers flexibility not only in intensity profiles but also in their three-dimensional (3D)

helical phase structures. Typically, linearly polarized light exhibits oscillations in the amplitude of the electric field while maintaining a transverse phase of polarization along one axis. The transverse plane lies in the $xy$ plane with the propagation direction along the $z$ axis. In contrast, light carrying SAM, such as circularly polarized light, features a rotating transverse phase of polarization and a nonvanishing electric field amplitude. Light carrying OAM exhibits a time-dependent 3D helical phase structure, also with a nonvanishing electric field amplitude except for the place with singularities of transverse phase. In this work, we use a particular type of OAM-carrying beam—an LG beam. Each LG transverse mode is described by the Laguerre polynomial $L_p^l(f(r))$, where $p$ is the RO and $l$ is the azimuthal index representing the OAM quantum number. The expression for the amplitude of the electric field of an LG mode is given by [28,29]

$$u_{l,p}(r,\varphi,z) = E_0 C_{\mathrm{pl}} \left[\frac{\sqrt{2}r}{w(z)}\right]^l \frac{w_0}{w(z)} \text{Ł}_p^l\left(\frac{2r^2}{w^2(z)}\right) \cdot e^{-i\phi_{\mathrm{pl}}(z)+i\frac{kr^2}{2q(z)}+il\varphi}. \quad (3)$$

Here, $p$ determines the number of rings related to the spatial intensity of light and $l$ controls the number of twists of the phase front. The constant $C_{\mathrm{pl}} = \sqrt{2p!/\pi(p+|l|)!}$ is used to normalize the amplitude.

The $z$-dependent radius of the beam spot is equivalent to $w(z) = w_0\sqrt{(z^2+z_R^2)/z_R^2}$ with the beam waist $w_0$ and the Rayleigh distance $z_R = k\omega_0^2/2$, where $k$ is the wave number. The imaginary terms inside the exponential function include the first term that is related to the Gouy phase $\phi_{\mathrm{pl}}(z) = (2p + |l| + 1)\arctan(z/z_R)$, the second term $\exp ikr^2/2q$ is related to the radius of curvature with $q(z) = z - iz_R$, and the third term $\exp il\varphi$ provides spiral wave front via controlling temporal phase delay $l\varphi$ around the azimuthal angle $\varphi$. The wave number $k$ is $2\pi/\lambda_{\mathrm{EM}}$, where the wavelength is $\lambda_{\mathrm{EM}} = c\tau_{\mathrm{EM}}$ and the period of light is $\tau_{\mathrm{EM}}$. In the focal plane, i.e., $z = 0$, the radius of the spot is $w(z) = w_0$, the Gouy phase is 0, and the curvature term $\exp ikr^2/2q(z)$ becomes the Gaussian distribution $\exp -r^2/w_0^2$. Throughout this paper, we consider that the sample is placed in the focal plane, and the angular frequency of light $\omega_{\mathrm{EM}}$ (hereafter referred to as frequency) is $2\pi/\tau_{\mathrm{EM}}$.

Considering the case with polarization along $x$ and $y$ directions and frequency $\omega_{\mathrm{EM}}$, the electric field of light carrying SAM number $s$, and the previously mentioned $l$ and $p$, is formulated as

$$\boldsymbol{E}_{\mathrm{EM}}(\mathbf{r},t) = u_{l,p}(r,\varphi,z)\cdot e^{-i(\omega_{\mathrm{EM}}t-\varphi_{t0})}\begin{pmatrix}\cos\varphi_{xy}\\ e^{-i\sigma}\sin\varphi_{xy}\end{pmatrix}\begin{pmatrix}\hat{\mathbf{e}}_x\\ \hat{\mathbf{e}}_y\end{pmatrix}, \quad (4)$$

where $\varphi_{t0}$ is the temporal phase at $t = 0$, $\varphi_{xy}$ is a constant of azimuthal angle that offsets the polarization along $xy$ plane, and $\sigma = s\cdot\pi/2$. For linear polarization (LP), $s$ is an even number, while for circular polarization (CP), $s$ is odd. Specifically, we use $s = 0$ for LP, $s = 1$ for left-handed CP, and $s = -1$ for right-handed CP. We use the notation $\mathrm{LG}_{\mathrm{pl},s}$ to denote the mode of the LG beam. The parameters of the LG beams used throughout this work are listed in Table I.

The vector potential $A_{\mathrm{EM}}$ of structured light in free space is given by $E_{\mathrm{EM}}/i\omega_{\mathrm{EM}}$. The time-dependent out-of-plane magnetic field, $B_z(r,t)$, is defined by the $z$ component of the curl of vector potential:

$$B_z(\boldsymbol{r},t) = (\nabla\times\boldsymbol{A}_{\mathrm{EM}})_z. \quad (5)$$

For light beams without OAM, such as the LP Gaussian beam $\mathrm{LG}_{00,0}$ and CP Gaussian beam $\mathrm{LG}_{00,\pm1}$, the structured distribution induces a time-dependent $B_z(\boldsymbol{r},t)$, which is proportional to the curl of amplitude distribution of $\boldsymbol{E}$ (see Ref. [20]). For light beams carrying OAM, the azimuthal phase factor $\exp il\varphi$ introduces additional contributions to $B_z(\boldsymbol{r},t)$ (see discussion in Appendix A). Snapshots of the electric field and resulting $B_z(\boldsymbol{r},t)$ for different combinations of SAM and OAM are shown in Figs. 9–11. The behavior of $B_z$ follows the distinct patterns for $s = -1, 0, 1$:

(1) $s - l = 0$. Both QNs $s$ and $l$ contribute to the rotational properties of light. According to Eqs. (3) and (4), the signs of the terms $il\varphi$ and $-i\sigma$ in the phase determine the opposite directions of rotation. When $s = l$, $B_z$ oscillates. For $s = l = 0$, it shows a strong linear movement (the absolute value of $B_z$ has twofold symmetry), while for $s = l = 1$, $B_z$ exhibits cylindrical symmetry.

(2) $s = 0$, $l > 1$. In this case, the light carries OAM, but remains LP at each moment. The electric field forms a $2l$-fold rotational flower pattern with radial symmetry, while the $B_z$ field is more complicate, resembling a vertical petal-shaped array. Based on the numerical results from Fig. 9, the dynamics of $B_z$ can be simplified as a spinning petal-shaped array.

(3) $s \neq 0$, $l \neq s$. In this case, the light carries both SAM and OAM, resulting in a more complex electric field. The electric field deforms between radial polarization and spiral polarization alternatively. For high-order OAM (e.g., $l > 1$ or $l < -1$), the radial and spiral polarizations interweave, forming a pattern with $(|l-s|)$-fold symmetry. As a result, the $B_z$ field behaves like a spinning plate with a flowerlike shape, also exhibiting $(|l-s|)$-fold symmetry.

Furthermore, the type of $B_z$ indicates how superconducting states are stirred. In the context of vortex generation, the characteristics of $B_z$ help to elucidate vortex dynamics. The numerical results for the $B_z$ profiles are presented in Appendix A.

### C. Simulation conditions

In our simulations, we focus on SC thin films with thickness $d \ll \xi$, where $\xi$ is the SC coherence length. As a result, we can disregard variations in the order parameter, current, and vector potential (such as due to absorptance) along the $z$ direction. Additionally, we neglect screening effects by assuming the London penetration depth or Pearl length is much larger than the coherence length, and at least longer than one of the sample size and the light spot size.

In type-II SCs, the coherence length $\xi$ is typically shorter than the Pearl length $\Lambda$ [30] or the London penetration depth $\lambda_L$ [31]. Based on this, we adopt niobium (Nb) thin films as a prototype for simulations. According to Refs. [32,33], a 2 nm Nb thin film has $\xi$ in the range 10−100 nm and $\Lambda$

TABLE I. The setting of LG beams mentioned in Secs. III A and III B.

| Light source | $s$ | $l$ | $p$ | $\phi_{t0}$ | $\phi_{xy}$ | Description |
|---|---|---|---|---|---|---|
| $LG_{00,0}$ | 0 | 0 | 0 | 0 | 0 | LP Gaussian beam without SAM and OAM ($x$ polarization in this work) |
| $LG_{00,\pm1}$ | $\pm1$ | 0 | 0 | 0 | $\pi/4$ | CP Gaussian beam with only SAM ($+/-$ for left/right-handed circular polarization) |
| $LG_{01,0}$ | 0 | 1 | 0 | 0 | 0 | LP LG beam with only OAM |
| $LG_{01,\pm1}$ | $\pm1$ | 1 | 0 | 0 | $\pi/4$ | CP LG beam with SAM and OAM |
| $LG_{0l,0}$ | 0 | $l>1$ | 0 | 0 | 0 | LP LG beam with higher order of OAM |
| $LG_{0l,\pm1}$ | $\pm1$ | $l>1$ | 0 | 0 | $\pi/4$ | CP LG beam with higher order of OAM |
| $LG_{pl,0}$ | 0 | $l$ | $p>0$ | 0 | 0 | LP LG beam with high radial order |
| $LG_{pl,\pm1}$ | $\pm1$ | $l$ | $p>0$ | 0 | $\pi/4$ | CP LG beam with high radial order |

in the range $1-500\,\mu$m. This allows us to use in simulations electromagnetic (EM) waves at frequencies up to tens of THz without considering screening effect, as the beam spot size of the beam has to be on the order of the wavelength [20]. Unless specified otherwise, the simulations assume SC thin films with $L = 25-30\xi$ and $d = 0.02\xi$, which for $\xi = 100$ nm [32,33] corresponds to $L = 2.5-3\,\mu$m and $d = 2$ nm. The size of the samples is deliberately reduced to enhance computational efficiency. This is specific to the simulation setup and not indicative of real-world application constraints.

Additionally, the sample size $L$ is chosen to be sufficiently large to avoid edge effects [20], particularly for light beams with higher RO number. The beam spot size $2w_0$ is fixed at $12\xi$. The intensity of light varies with each quantum number, which will be discussed later. In Appendix B, we provide the values of $E_0$ used in the simulations and the corresponding sample size $L$, except for the specific cases that are mentioned in the figure captions. The length of the edge of the mesh in the simulations is smaller than $\xi$, which is discussed in Appendix B. $E_0$ and $L$ are expected to lie in the ranges of kV/cm–MV/cm and micrometers, respectively, based on previous work [20]. Besides, we set $\gamma = 10$ for the simulation.

## III. RESULTS

### A. Spin and orbital angular momentum

Light carrying SAM and OAM imparts rotational and revolving orbital motion to the superconducting coherent state. Vortex generation through the AM transfer from an electromagnetic beam during processes of hot spot quenching and superconducting condensate formation has been explored in Refs. [34,35]. In contrast, our previous work [20] demonstrates that vortices can also be generated without the need for AM transfer, and independent of the quenching process. The resulting out-of-plane $B_z$ induces and stirs the supercurrent, affecting both the fast response of $\theta_s$ and the slower reaction of $|\psi|$ [20]. In this section, we begin by examining five simple cases of SAM and OAM, $(s, l) = (0, 0), (1, 0), (0, 1), (-1, 1)$, and $(1, 1)$, to explore the transfer of AM from light to vortices. Following our previous work [20], we use the light frequency at $\omega_{EM} = \omega_{GL}/40$ to allow sufficient time for the generation and recombination of VPs.

#### 1. Imprint effect of supercurrent

In the standard TDGL model, the unit time of system $\tau_{GL}$ is determined by the relaxation time of the supercurrent [36], while the relaxation time of the order parameter is $u$ times longer than $\tau_{GL}$. In the gTDGL model, the relaxation time of the order parameter is even longer. When considering the relaxation times of $|\psi|$ and $\theta_s$ induced by the optical pulse, they can be $\sim 30\tau_{GL}$ and $\sim 1.5\tau_{GL}$ for $\gamma = 10$, respectively (see Appendix B in previous work [20]). These timescales are typically on the order of picoseconds for the materials listed in Ref. [20] when $T$ is close to $T_c$. It clearly demonstrates the rapid response of the supercurrent and $\theta_s$, followed by the delayed response of $|\psi|$. The structured light imprints its effects first on the supercurrent directly, and induces the striped structure on $\theta_s$ before vortex generation, with the longest lasting influence observed in $|\psi|$.

If we define the curl operator as representing the vorticity of a physical parameter, then $B_z$ can be interpreted as the vorticity of the vector potential, as expressed in Eq. (5). Figures 13–15 in Appendix C provide the numerical evidence that the vorticity profile of the supercurrent density $\omega_{v,s} = (\nabla \times \boldsymbol{J_s})_z$ directly inherits its structure from the $B_z$ field, occurring before vortex generation. Assuming that the contributions to the phase of the order parameter $\theta_s$, including pure supercurrent component $\theta_{s,Js}$ and vortex component $\theta_{s,V}$, can be separated, i.e., $\theta_s \approx \theta_{s,Js} + \theta_{s,V}$, and neglecting the contribution from the variation in the amplitude of the order parameter, the total vorticity of the supercurrent $\boldsymbol{J_s} = \mathrm{Im}[\psi^*(\nabla - i\boldsymbol{A})\psi] = |\psi|^2(\nabla\theta_s - \boldsymbol{A})$ [see Eq. (2)] can be approximated as

$$\begin{aligned}\nabla \times \boldsymbol{J_s} &\approx |\psi|^2 \nabla \times (\nabla\theta_s - \boldsymbol{A}) = |\psi|^2(\nabla \times \nabla\theta_s - \nabla \times \boldsymbol{A}) \\ &\approx |\psi|^2(\nabla \times \nabla\theta_{s,Js} + \nabla \times \nabla\theta_{s,V} - \nabla \times \boldsymbol{A}). \qquad (6)\end{aligned}$$

Since the phase $\theta_{s,Js}$ provides the continuous part of the phase, the first term in the brackets in the last line of Eq. (6) turns out to be $\nabla \times \nabla\theta_{s,Js} = 0$. The second term is a nonzero value due to the singularity point of $\theta_{s,V}$ in vortex. The third term is equivalent to $-\boldsymbol{B}$ according to Eq. (5). Hence, before the vortex generation, the vorticity of supercurrent can be rewritten as

$$\omega_{v,s} = (\nabla \times \boldsymbol{J_s})_z \approx -|\psi|^2(\nabla \times \boldsymbol{A})_z = -|\psi|^2 B_z. \qquad (7)$$

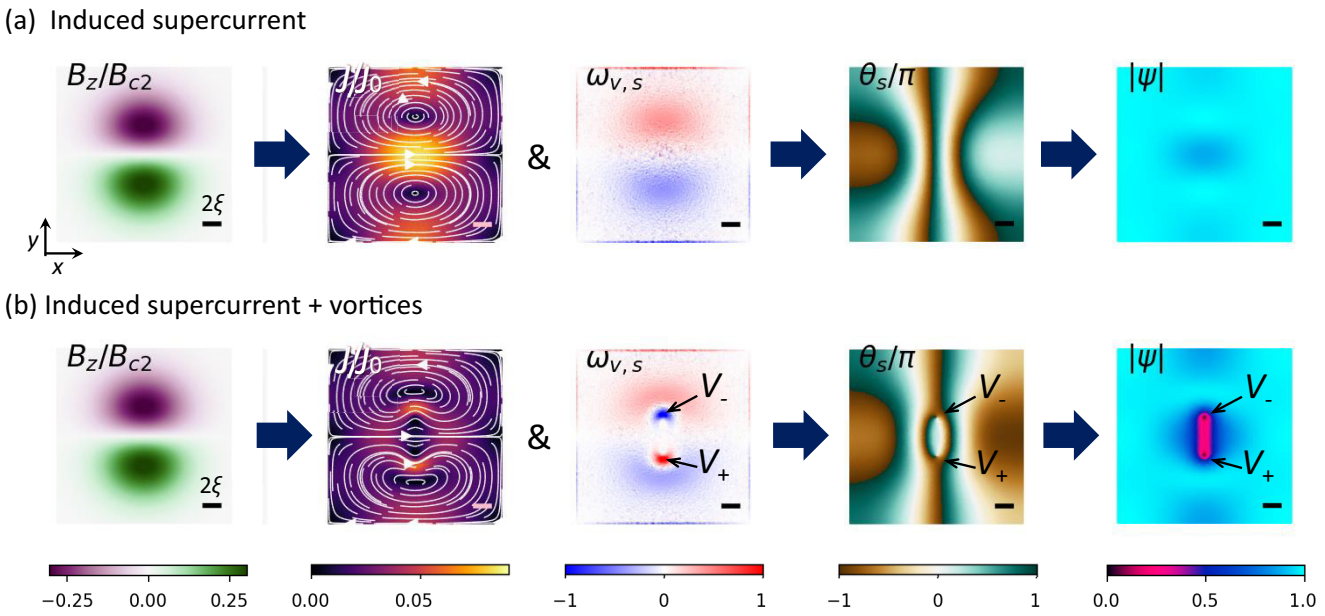



FIG. 2. Different profiles showing the effects of optically induced supercurrents and vortices. These profiles include out-of-plane magnetic field $B_z$, supercurrent density $J_0$, vorticity of supercurrent density $\omega_{v,s}$, phase of the order parameter $\theta_s$, and amplitude of the order parameter $|\psi|$, from left to right. The arrows indicate the structure transferring from $B_z$ of light through $J_0$, normalized $\omega_{v,s}$, $\theta_s$, to $|\psi|$. The snapshot in panel (a) shows the $LG_{00,0}$-induced supercurrent before vortices generation at $t = 10\tau_{GL}$, while panel (b) shows the state after vortices generation at $t = 90\tau_{GL}$. The notations $V_+$ and $V_-$ represent vortex and antivortex, respectively.

The proof in Eqs. (6) and (7) directly demonstrate the imprinting effect, where the vorticity of the vector potential is transferred to the vorticity of the supercurrent, leading to the observed dynamics.

We demonstrate this in Fig. 2, where snapshots of the superconducting states and magnetic fields at times before and after generation of a VP are shown for the case of linearly polarized light. In Fig. 2(a), the vorticity $\omega_{v,s}$ of the supercurrent is shown as a faint red area for positive vorticity and a faint blue area for negative vorticity. The resemblance between plots for $B_z$ and $\omega_{v,s}$ is clearly visible. This resemblance persists for all types of structured light (Appendix C). After the vortices emerge, the vorticity manifests as bright red or blue dots, representing vortices ($V_+$) and antivortices ($V_-$). The profile of $\theta_s$ shows singularity points with opposite winding numbers, while the profile of $|\psi|$ exhibits zeros at the location of the vortices.

In contrast to the profile of the supercurrent, the motion of vortices is more complex and unpredictable. Therefore, in the following discussion, we will focus on the dynamics of vortex motion.

#### 2. *Imprint effect of spin angular momentum s*

As was in details shown in the case of linearly polarized light, $LG_{00,0}$, the VPs are generated due to oscillating in time locally nonzero $z$ component of the magnetic field that changes sign spatially and creates regions of positive and negative magnetic fluxes. When these fluxes are greater than the magnetic flux quantum $\Phi_0$, VPs might be generated. Vortex dynamics for several cases of light carrying SAM and OAM is shown in Fig. 3. The light sources $LG_{00,0}$ and $LG_{00,\pm1}$ serve as the first examples, both exhibiting similar transient $B_z$ profiles but with different dynamical behaviors. The former carries zero AM as an LP beam, while the latter carries SAM $s = 1$ for left-handed CP and $s = -1$ for right-handed CP. As shown in Fig. 9, LP $LG_{00,0}$ exhibits oscillating dual-semicircle patterns in $B_z$, whereas CP $LG_{00,\pm1}$ displays spinning dual-semicircle patterns in $B_z$ with constant field intensity. Figure 3 illustrates the results for the vortex dynamics in panel (a) for $LG_{00,0}$ and panel (b) for $LG_{00,1}$, also presenting snapshots of the order parameter amplitude $|\psi|$, phase $\theta_s$, and vorticity of the current $\omega_{v,s}$. The vortex time traces are defined by the regions where $|\psi| < 0.05$ with the sign of vorticity distinguishing the vortex (red) and the antivortex (blue).

The vortex motion exhibits distinct characteristics depending on the light beam. LP $LG_{00,0}$ generates staggered VPs that appear and disappear periodically, with intervals between the processes of generation and recombination [as seen in Fig. 3(a)]. In contrast, CP $LG_{00,1}$ produces a braiding VP [as shown in Fig. 3(b)] without recombination. Due to SAM, the vortices in the VP induced by $LG_{00,1}$ also spin around their point of origin. The vortex dynamics induced by LP $LG_{00,0}$ have been thoroughly discussed in our previous work [20]. In contrast, for light carrying SAM, unlike the case of zero AM, once the system begins to rotate, the braided VP can move perpetually, presenting a "yin-yang" pattern of vorticity comprised of the opposing vorticity of the vortices of the VP within the supercurrent. The evolution of the VPs is further clarified by their projection on the $xy$ plane, which shows linear scars (or the trace/traces of vortices) for the LP $LG_{00,0}$ beam and circular scars for the CP $LG_{00,1}$ SAM beam. The complete dynamics of the superconducting condensate for the cases of $LG_{00,0}$ and $LG_{00,\pm1}$ sources are demonstrated in Videos S1, S2, and S3 in the Supplemental Material [26].

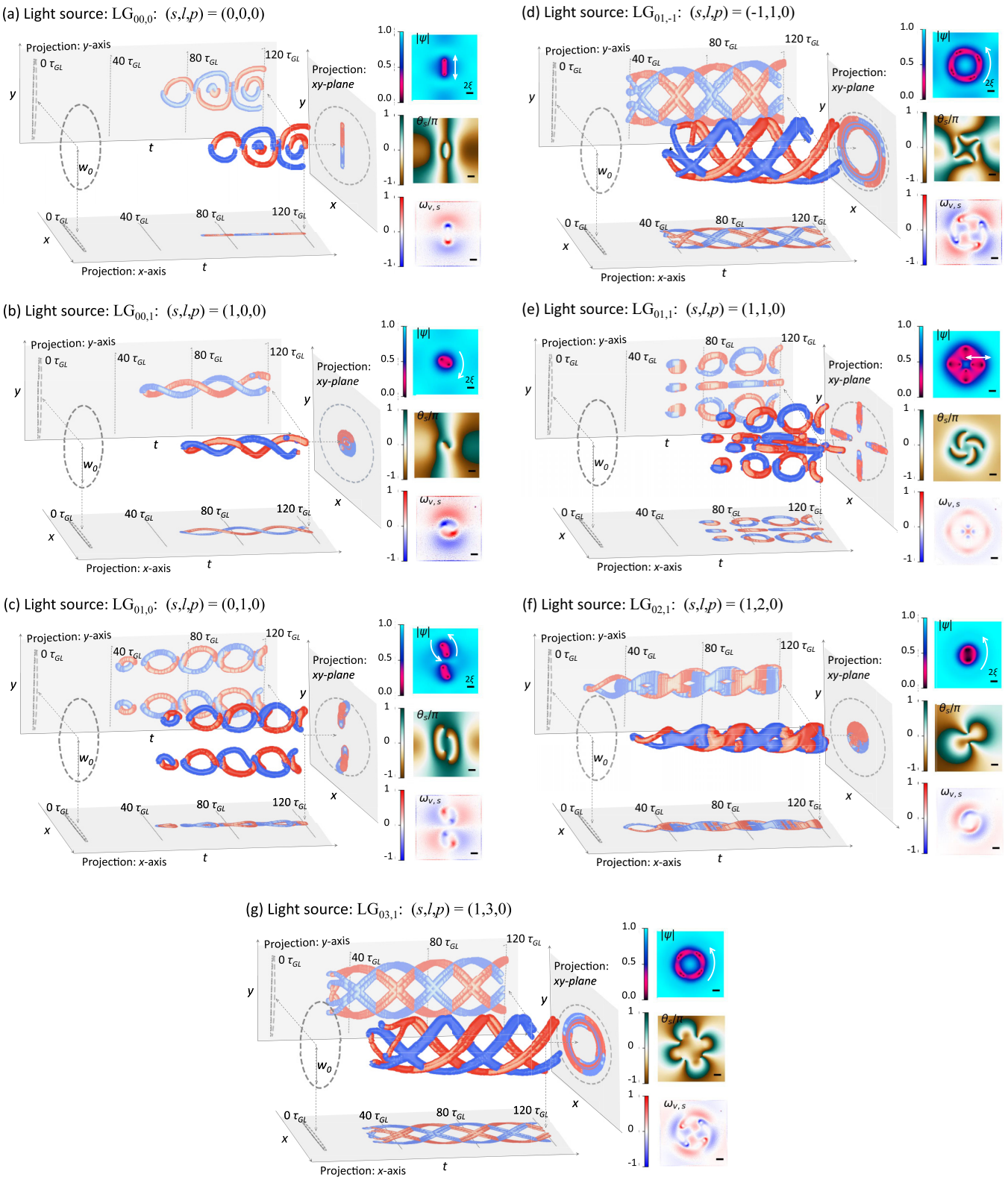



FIG. 3. Time trace of vortices and snapshot of the order parameters induced by light sources: (a) LP LG$_{00,0}$, (b) CP LG$_{00,1}$, (c) LP LG$_{01,0}$, (d) CP LG$_{01,-1}$, (e) CP LG$_{01,1}$, (f) CP LG$_{02,1}$, and (g) CP LG$_{03,1}$. We illustrate the time-varying 2D traces of vortices. Each time frame of 2D vortex traces is displayed along vertical slices, like the orientation of the "projection of $xy$ plane," while the horizontal direction corresponds to the evolution in time. The red and blue curves depict the trace of vortices and antivortices, respectively. The inserts of $|\psi|$, $\theta_s$, and $\omega_{v,s}$ are the snapshot of amplitude of order parameter, phase, and vorticity of the supercurrent, respectively. The full motion records are available in Videos S1, S2, and S3 in the Supplemental Material [26].

#### 3. Imprint effect of orbital angular momentum l

OAM, which imparts a revolving motion to light rather than spinning, affects the order parameter and superflow in a distinct way. The rotational phase factor $\exp il\phi$ around the center leads to a null electric field at the beam's center and contributes to oscillating in time $B_z$. In Fig. 3(c), we present the time evolution of vortices and order parameters induced by light carrying pure OAM, $l = 1$. The vortex traces and $|\psi|$ display two linearlike motions of VPs in the upper and lower ($y \gtrless 0$) half planes.

The mechanism of vortex generation in this context parallels the process observed in vortex generation induced by linearly polarized light [20], where vortices and antivortices emerge from regions with zero magnetic field, $B_z = 0$, positioned between the maxima and minima of $B_z$. However, instead of generating a branch cut between paired vortices, each vortex in this configuration links its branch cut to the vortex located in a different VP. This arrangement makes the phase profile $C_2$ rotationally symmetric about the $(x = 0, y = 0)$ point (center of the sample). During the vortex generation, the rotating magnetic field component $B_z$ "tears up" the phase from the left and right sides, and further displaces the phase between them, like the shear force along the $x = 0$ line (transform boundary). In Fig. 16(a) (see Appendix D), we demonstrate the phase displacement and subsequent VP formation, while Fig. 16(b) shows the phase recovering as the VPs recombine.

Combining OAM and SAM introduces more complexity. In the case of the beam with the OAM number $l = 1$ paired with the left- or right-handed CP, the resulting patterns of both $B_z$ and the vortex dynamics vary significantly. For $s = -1$, $\mathrm{LG}_{01,-1}$, when the SAM aligns with the OAM, $B_z$ exhibits a twofold rotational symmetry due to $l - s = 2$. Figure 3(d) and Video S2 in the Supplemental Material [26] present the vortex motions and dynamical simulation results. Vortex generation begins with four VPs around the ring orbital, continuing in a perpetual revolving motion. Besides, the resulting $\theta_s$ profile shows concave branch cuts.

For the case of $s = 1$, $\mathrm{LG}_{01,1}$ corresponds to the opposite directions of SAM and OAM. The vortex motion and a snapshot of the SC state are presented in Fig. 3(e), and the vortex motions and full dynamics of the SC condensate are provided in Video S3 in the Supplemental Material [26]. The electric field $\boldsymbol{E}$ exhibits dynamical changes between the radial and spiral polarizations, whereas oscillating in time $B_z$ is rotationally symmetric with a nodal line (circle at which $B_z = 0$). Interestingly, the vortices move linearly, similar to the vortex motion induced by linear light [see Fig. 3(a)], but are distributed radially. In contrast, the branch cuts in the SC phase profile alternate between radial and spiral alignment, resembling the behavior of $\boldsymbol{E}$ of the light beam. The spinning nature appears to be concealed in the $\theta_s$ profile and remains invisible in $|\psi|$.

For this case, the resulting linear motion of vortices in the VPs can be explained using the concept of inverse trammels (see details in Appendix D). The traditional trammel method provides a way to plot a circular (or elliptical) trajectory using linear motion. In the vortex generation case for $s = l = 1$, when the amplitude $E_0$ is sufficient to generate four VPs (the minimum number of VPs $\mathrm{LG}_{01,1}$ can generate), $B_z$ field induces shift of phases along two intersecting lines, as shown by the gray cross in Fig. 17(a). The phase rotates along in these lines, driving the linear generation and recombination of VPs. The four occurring branch cuts are analogous to four trammels along the intersecting lines, effectively illustrating an inverse of trammel process, where circular motion is converted into linear motion. Additionally, $B_z$ shows a maximum at center of $\mathrm{LG}_{01,1}$, unlike $\mathrm{LG}_{00,0}$, which peaks at the sides. Notably, no vortex is present at the center for $\mathrm{LG}_{01,1}$. In Fig. 17(b), we capture the moment of VP generation as the phase branch cuts displace along the trammel trace (transform boundary), and VP recombination occurs as the displaced phases realign during the swinging motion of "phase trammels."

Moreover, the supercurrent $J_s$ and vorticity $\omega_{v,s}$ in Fig. 3(e) and Video S3 in the Supplemental Material [26] exhibit a clearly swirly supercurrent along the orbital, which behaves like in a closed-loop circuit, but it is purely induced by the light source $\mathrm{LG}_{01,1}$. The swirly supercurrent flips the sign immediately as $B_z$ changes the sign. This supercurrent behaves like a supervortex, which can also be found in the cases of $\mathrm{LG}_{11,1}$ (Video S6) and $\mathrm{LG}_{21,1}$ (Video S9) in the Supplemental Material [26].

Consequently, the results for $\mathrm{LG}_{01,1}$ and $\mathrm{LG}_{01,-1}$ suggest that the QNs of SAM and OAM are interconnected in light and cannot be treated independently. While the supercurrent and vortex motion are not directly related to the QNs, they are more easily associated with the behavior of $B_z$. Additionally, the formation of vortices requires a minimum number of VPs, implying that a higher field intensity $E_0$ is necessary for their generation. In the next section, a general case for QNs will be discussed, offering a broader perspective on imprinting.

#### 4. Higher order of orbital angular momentum

*(a) Quantum numbers* $l > 1, s = 0$. Figure 4(a) shows the SC states induced by pure OAM-carrying light sources. From $l = 1$ to $l = 5$, various vortex traces appear in the $|\psi|$ profile, resembling shapes such as colons, lightning bolts, and round brackets. When $l = 1, 2$, the transform boundary of the displacing phase is still observable. For $l > 2$, the vortex traces stabilize into round bracketlike shapes. However, in the SC phase profile, the transform boundary becomes difficult to be identified as shear lines associated with these round bracket traces. Despite not forming complete circular patterns, the vortices continue to move counterclockwise, following the rotational direction of the OAM.

*(b) Quantum numbers* $l > 1, s \neq 0$. When SAM is present, both $\boldsymbol{E}$ and $B_z$ exhibit $(|l - s|)$-fold rotational symmetry, with the sign of $(l - s)$ determining the direction of rotation: negative for right-handed (counterclockwise) and positive for left-handed (clockwise). Figures 4(b) and 4(c) show $B_z$ for QNs $l > 1, s = -1$ and $l > 1, s = 1$ along with the corresponding imprinted SC states, respectively. Aside from the ring size affected by $l$, this symmetry is directly imprinted on the profiles of $\omega_{v,s}$ and $\theta_s$. The vortices in $|\psi|$ display the $(2|l - s|)$-fold symmetry because vortices and antivortices are indistinguishable in $|\psi|$. From a symmetry perspective, both

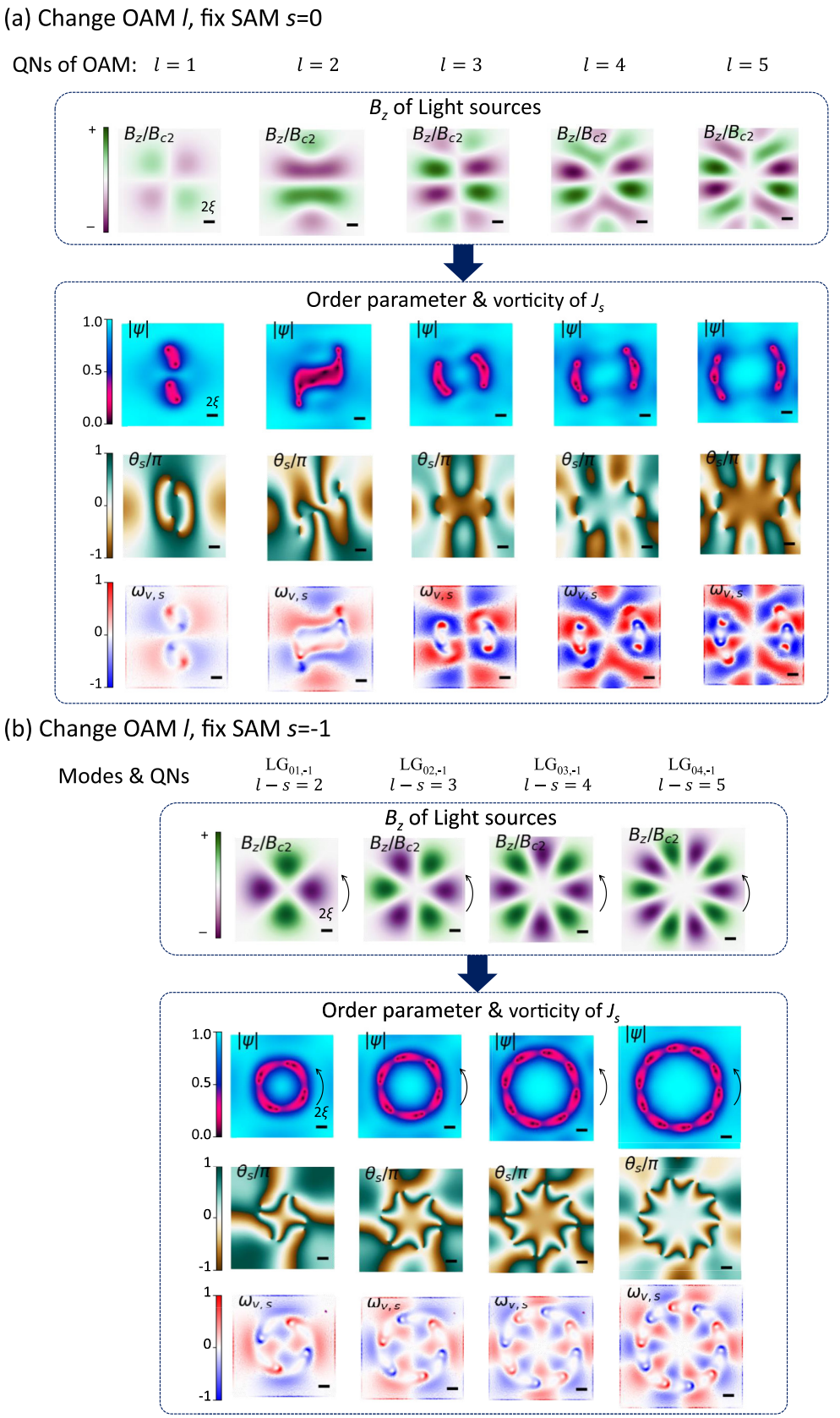



FIG. 4. Snapshot of $B_z$ and order parameters induced by higher-order OAM-carrying light sources of quantum numbers (a) from $l = 1$ to $l = 5$ at $t = 90\tau_{GL}$, (b) with left-handed CP at $t = 120\tau_{GL}$, and (c) with right-handed CP at $t = 120\tau_{GL}$. The imprinted SC states are shown in the lower block, including $|\psi|$, $\theta_s$, and normalized $\omega_{v,s}$ from top to bottom as labels. Details of the applied electric fields are provided in Appendix B. The complete records of the vortex dynamics are available in Videos S1, S2, and S3 in the Supplemental Material [26].

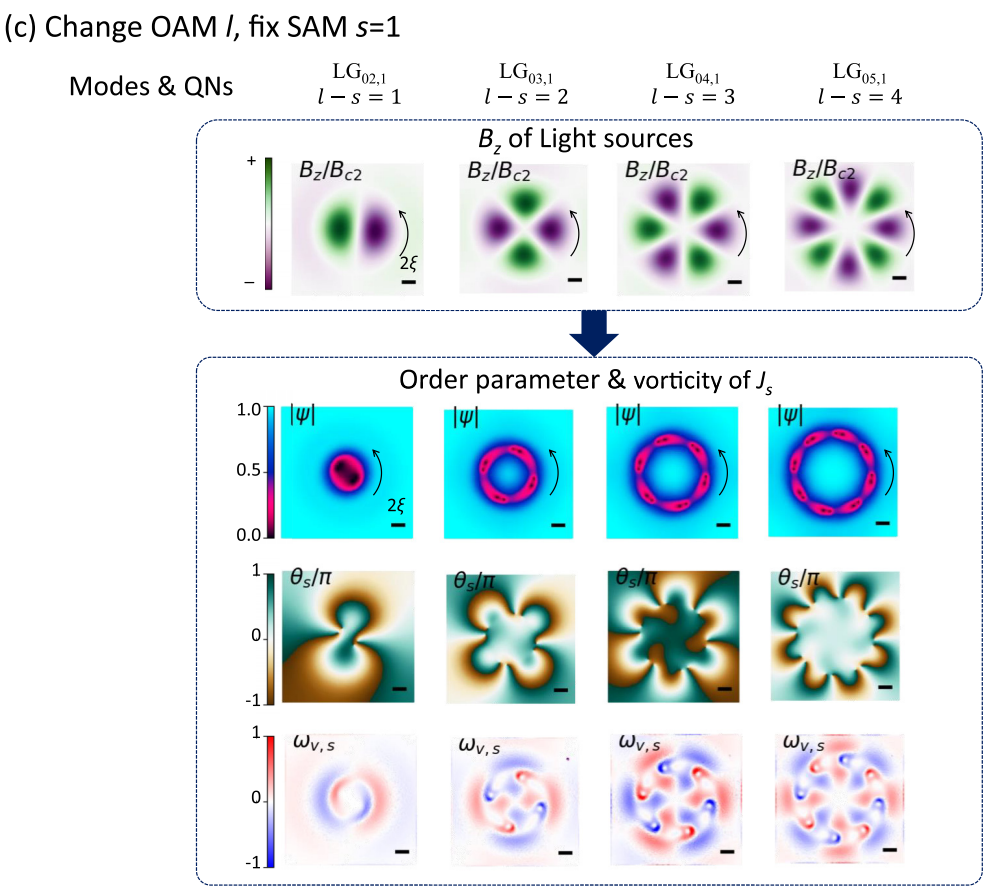



FIG. 4. (*Continued*.)

$s = -1$ (left-handed CP) and $s = 1$ (right-handed CP) behave similarly when $(l - s)$ are the same.

*(c) Convex and concave curves of phase branch cuts.* Analyzing the cases where $(l - s) = 2, 3, 4$ in Figs. 4(b) and 4(c), we find that the profiles of $|\psi|$ and $\omega_{v,s}$ appear nearly identical for the same $(l - s)$ values, with only minor differences in the ring size. However, the phase profiles reveal distinctly different features. Both configurations maintain $(|l - s|)$-fold symmetry with singularity points aligned along the ring orbitals. For $s = -1$, the phase exhibits concave phase branch cuts between each VPs, curving inward toward the inner ring. Conversely, when $s = 1$, the phase shows the convex phase branch cuts between the VPs, curving outward toward the outer ring. This difference in phase structure may influence the size of the rings: The convex branch cuts compress the ring, while the concave branch cuts can cause the ring orbital to expand.

Both $s = -1$ and $s = 1$ cases exhibit kaleidoscopic profiles for $\theta_s$, with distinctive features both inside and outside the ring that enrich the overall pattern. The phase branch cuts cause patterns with a high contrast ratio along the ring, in stark contrast to the smooth patterns outside of it. Within the region surrounded by the phase branch cuts, plateau ($\theta_s \nsim 0$) or valley ($\theta_s \sim 0$) structures maintain rotational symmetry. The feature of the outer phase rotates as the vortex moves, while the inner plateau structure oscillates in amplitude during the revolution of the VPs. These components complicate the phase structure, yet they are nearly muted in the $|\psi|$ profile. Due to these characteristics, the $\theta_s$ profile for $s = -1$ results in an $(|l - s|)$-fold star-shaped phase, while $s = 1$ yields an $(|l - s|)$-fold flower-shaped phase. The complete dynamics is displayed in Videos S2 and S3 in the Supplemental Material [26].

*(d) Vortex rings and vortex droplet rings.* In addition to the phase structure, distinct vortex structures can be observed in the profiles of $|\psi|$. For the cases of $LG_{02,1}$ and $LG_{03,1}$, each node of the ring exhibits two singularity points in the $\theta_s$ profile. However, $LG_{02,1}$ contains one hole in the $|\psi|$ profile (i.e., the area of $|\psi| \sim 0$), while $LG_{03,1}$ has two holes. Based on the morphology of the order parameters, these behaviors can be classified as braiding vortex droplets for $LG_{02,1}$ and swirling two-dimensional (2D) vortex ring for $LG_{03,1}$.

The demonstration in Figs. 3(f) and 3(g) illustrates the vortex traces of both vortex droplets and vortices. Notably, aside from the quantity and size of vortices, the size of the orbital is a key factor influencing this morphology.

The formation of a vortex ring is shown in Fig. 5(a). During this process, vortices with the same vorticity "bond" together, which initially evolves from "bonding" VPs with different vorticities. The evolution of the vortex ring, as demonstrated in Figs. 5(a) and 5(b), captures the process of VP generation, where bonding $V_-$ and $V_+$ vortices are generated, debond, and then rebond again between $V_-$ and adjacent $V_-^*$. The duration of these bond-debond-rebond process of vortices occurs within $10\tau_{GL}$. Afterward, the ring of vortices stabilizes, with vortices of the same vorticity swirling consistently along

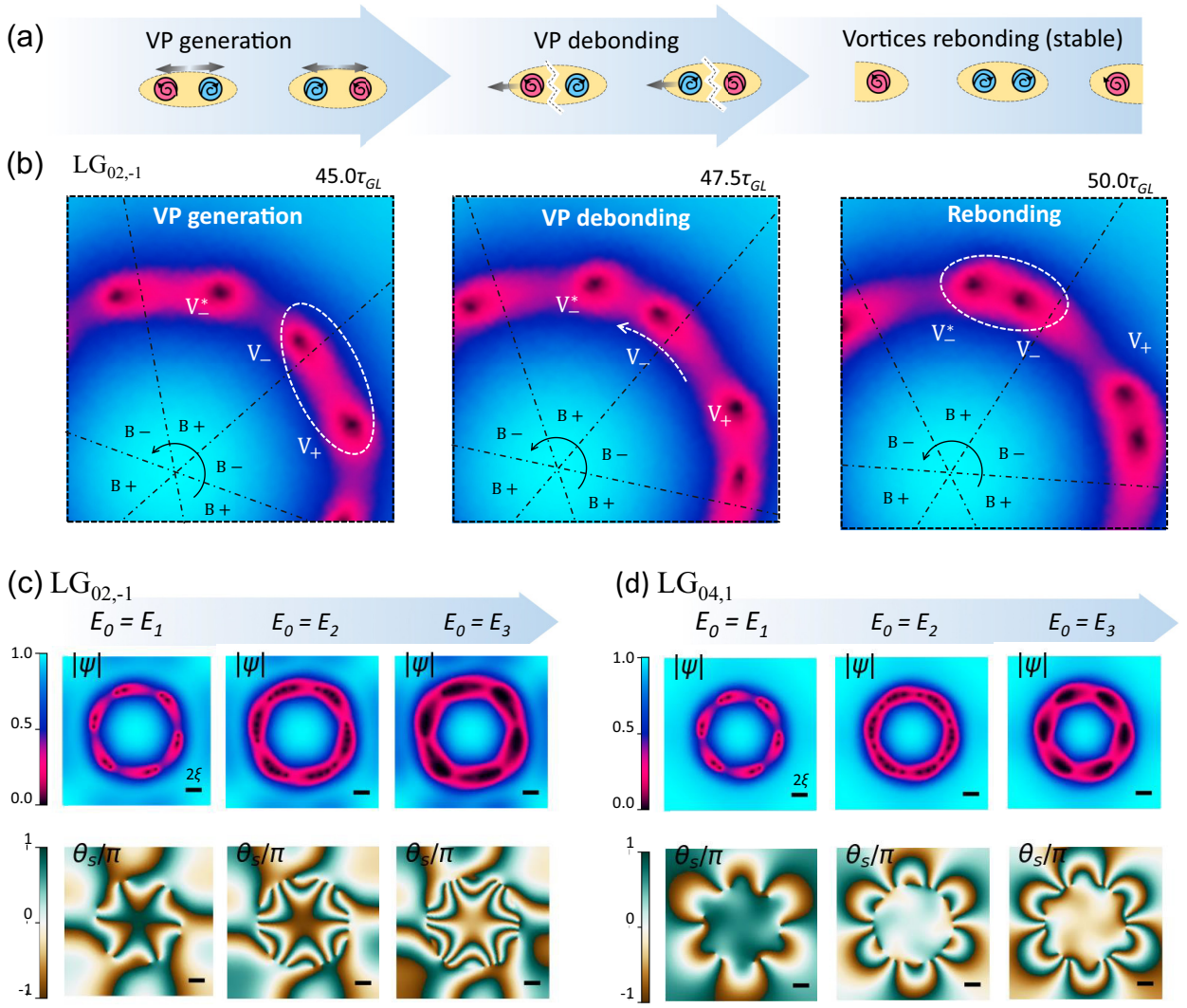



FIG. 5. Panels (a) and (b) are related to vortex debonding and rebonding process, and panels (c) and (d) are in regard to formation of vortex-droplet ring. (a) Schematic diagram of debonding and rebonding process. (b) Tracking the formation of vortex rings. The light source is $LG_{02,-1}$ for demonstration. Snapshots from top to bottom illustrate the bonding of $V_-$ and $V_+$, the debonding of $V_-$-$V_+$, and rebonding of $V_-$ with an adjacent $V_-^*$. The dash-dotted lines represent the boundaries between a positive $B_z$ lobe (marked B+) and a negative $B_z$ lobe (marked B−). Panels (c) and (d) are vortex ring and vortex-droplet ring induced by the same QN of the light source, but with varying $E_0$. The selected light sources are (c) $LG_{02,-1}$ for the star-shaped phase and (d) $LG_{04,1}$ for the flower-shaped phase. The electric field amplitudes $E_1 = 6.0A_0\omega_{GL}$, $E_2 = 8.0A_0\omega_{GL}$, and $E_3 = 10.0A_0\omega_{GL}$ are used to tune the state of the vortex ring. For $E_1$, $E_2$, and $E_3$, the ring consist of two vortices, four vortices, and vortex droplets, respectively. The rings rotate counterclockwise.

the orbital. The tendency for vortices of the same vorticity to group together can be likely attributed to the need to maximize the penetration of $B_z$ through the vortices. After the pairing of $V_-$ and $V_-^*$ as shown in the right part of Fig. 5(b), this pair stably follows the positive $B_z$ lobe. This phenomenon occurs in both vortex ring structures with star-shaped phase profiles (e.g. $s = -1, l \geqslant 1$ in Video S2 in the Supplemental Material [26]) and flower-shaped phase profiles ($s = 1, l \geqslant 3$ in Video S3 in the Supplemental Material [26]). This phenomenon is also found in the data for higher order ($p > 0$) in vortex rings as shown in Videos S5, S6, S8, and S9 in the Supplemental Material [26]. In the time traces of vortices demonstrated as a 3D plot in Figs. 3(d) and 3(g), this process can be observed in the initial stages of vortex generation as well.

Apart from the bond-debond-rebond process of vortices in the ring structures, we can observe this process in the cases of pure OAM light sources ($l \geqslant 3, s = 0$) as well. In Appendix E and Video S1 in the Supplemental Material [26], this process for $s = 0$ has starting and ending repetitively, which is unlike the case for the ring-shaped orbital with stable rebonding VPs. The bracket-shaped orbitals provide four end points and allow the existence of a transient "single vortices" at those end points. One vortex in the rebonding VP with the same vorticity recombines when it touches the vortex at the end point, as shown in Fig. 18.

Moreover, based on the hypothesis that the ring/orbital size influences the formation of vortex droplets and vortices, a ring with more vortices can transform into a ring of vortex droplets under certain conditions. Figures 5(c) and 5(d) demonstrate

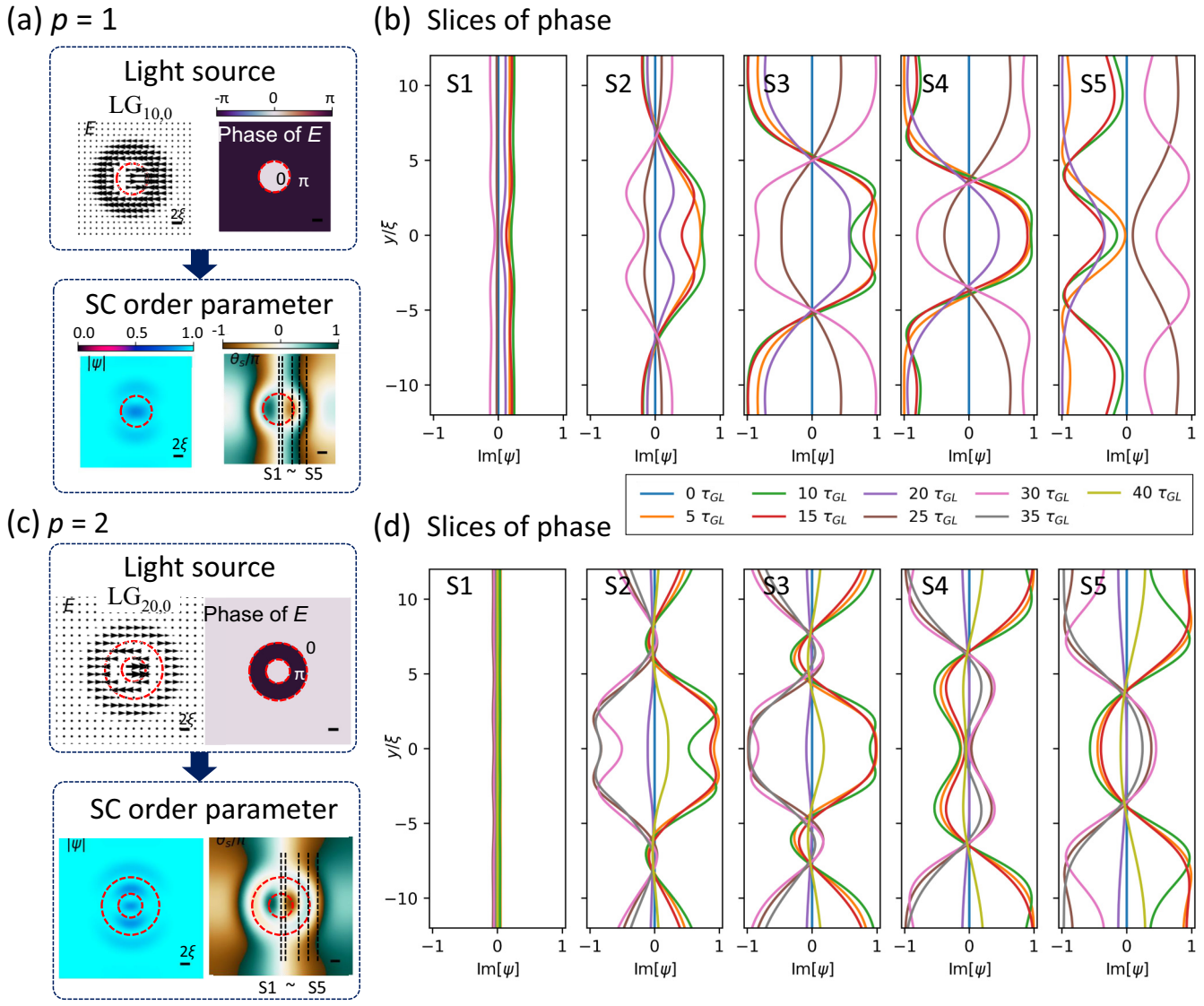



FIG. 6. The SC states induced by the $p$-carrying light are presented in this figure. Panels (a) and (b) display the results for $p = 1$, while panels (c) and (d) correspond to $p = 2$. The electric field and phase of $E$ are shown in the "light source" blocks in panels (a) and (c), while the "SC order parameter" blocks illustrate snapshots of $|\psi|$ and $\theta_s$. The red dashed rings indicate the locations of the discontinuity in the phase of $\boldsymbol{E}$. The black dashed lines labeled S1–S5 in $\theta_s$ mark the phase cuts used to demonstrate the standing wave in panels (b) and (d). Panels (b) and (d) show the imaginary part of Im$[\psi]$ along the cuts from S1 to S5. The different colors of the curves represent various times, as indicated in the legend between panels (b) and (d).

the progression from a ring of vortices to a ring of vortex droplets as the number of vortices increases, controlled by the amplitude of the electric field. As the number of vortices grows, the additional vortices follow the orbital path, extending the length of the chain of vortices with the same vorticity between the nodes. The nodes maintain the same $n$-fold symmetry in the $|\psi|$ profile. Additionally, the branch cuts arrange in parallel way rather than in series. This arrangement preserves the same $n$-fold star and flower symmetries and further results in multilayered star and flower patterns of $\theta_s$. Figures 5(c) and 5(d) demonstrate the increase in number of vortices in each chain from two to four.

As the electric field increases further, the vortices "merge" into a ring of vortex droplets, which can be observed in the profiles of both $|\psi|$ and $\omega_{v,s}$. In the $\theta_s$ profile, each branch cut remains distinct and visible. The overall profile remains the $(|l - s|)$-fold symmetric even if the number of vortices increases. Additionally, each droplet in the ring behaves similarly to the braiding vortex droplet, displaying a sharper edge at the front and a trailing tail at the back. In Appendix B, we demonstrate the corresponding meshgrid to inspect the capability of the simulation for spatial resolution of this phenomenon.

### B. Radial order $p$

In LG beams, the QN of RO, $p$, determines the number of rings in the intensity profile of the electric field. Interestingly, it also creates discontinuous phase boundaries for each ring in the phase profile of the electric field. When there is no

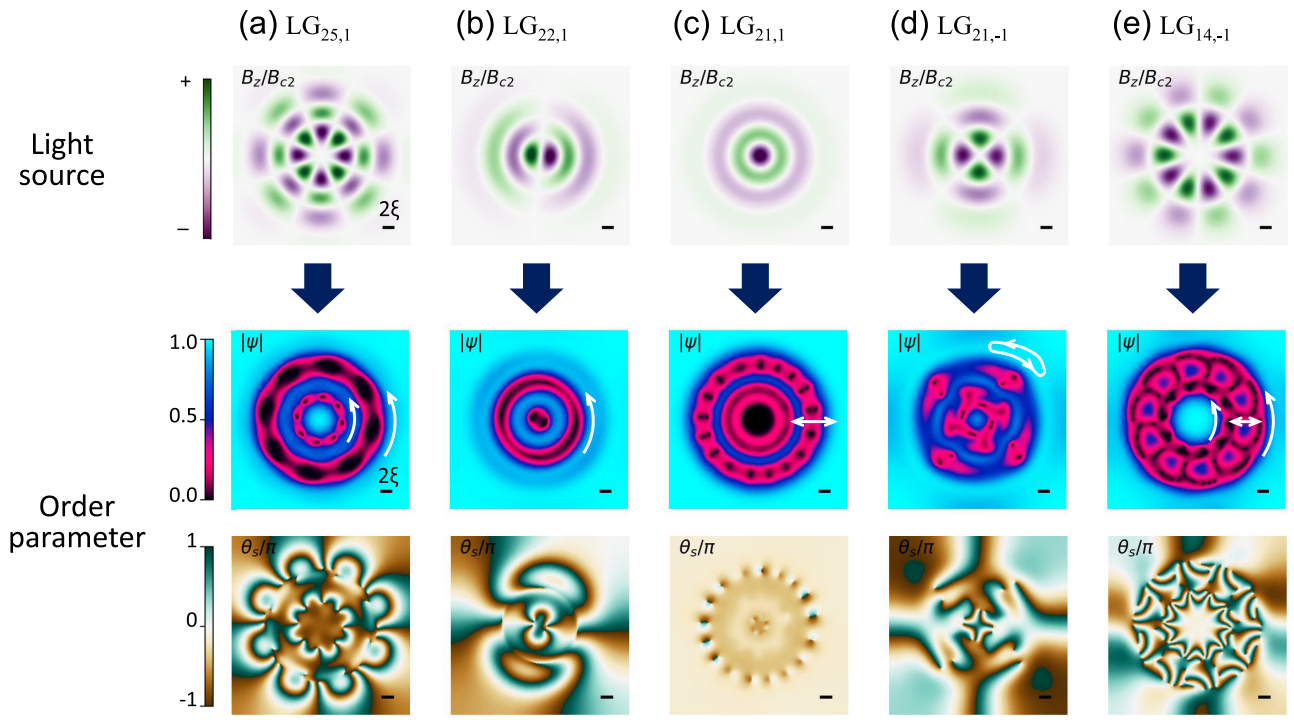



FIG. 7. Snapshots of the SC order parameter imprinted by light sources carrying both $p$ and AM. These include (a) $LG_{25,1}$ showing a multiring structure, (b) $LG_{22,1}$ exhibiting large gradient-phase-induced zero-$|\psi|$ curves, (c) $LG_{21,1}$ inducing a nonrotating vortex corral, (d) $LG_{25,-1}$ presenting abnormal motion of the outer vortex ring, and (e) $LG_{14,-1}$ showing interorbital interactions via vortices.

SAM and OAM, the rings exhibit a constant phase, with a $\pi$-phase deviation between adjacent rings, a phenomenon also known as the binary phase [37]. When $l$ is nonzero, the OAM introduces a phase change in the electric field that varies with the azimuthal angle. In this section, we will first examine the effects of $p$ in the context of pure binary phase and then extend our discussion to include the cases involving $s$ and $l$.

#### *1. Imprint effect of binary phase with p*

In this work, we investigate two cases of binary phase for the polarization of an electric field, specifically for $p = 1, 2$. In terms of the intensity profile of the electric field, the outer ring generates more linear VPs that are perpendicular to the polarization, as demonstrated in Videos S4 and S7 in the Supplemental Material [26]. Beyond the intensity, the discontinuous phase of the polarization creates a circle of singularity (nodal circle), significantly influencing the SC state. The snapshots of the binary phases are presented in Figs. 6(a) and 6(c).

The ring of discontinuity in the phase of the polarization imprints a ring of zero phase in $\theta_s$ of the SC state via $B_z$ prior to vortex generation. This ring causes the imaginary part of the order parameter, $\mathrm{Im}[\psi] = |\psi| \sin\theta_s$, to function as a drumhead for the order parameter. In our simulations, clear standing waves are observed at the edge of the "phase drum." For the case of $p = 2$, two rings of zero phase in $\theta_s$ manifest. When examining the cuts along the $y$ axis of $\mathrm{Im}[\psi]$, the $\theta_s$ profiles for $p = 1$ reveal two nodes of standing wave within the ring, as illustrated in Fig. 6(b), while $p = 2$ exhibits standing waves with four nodes.

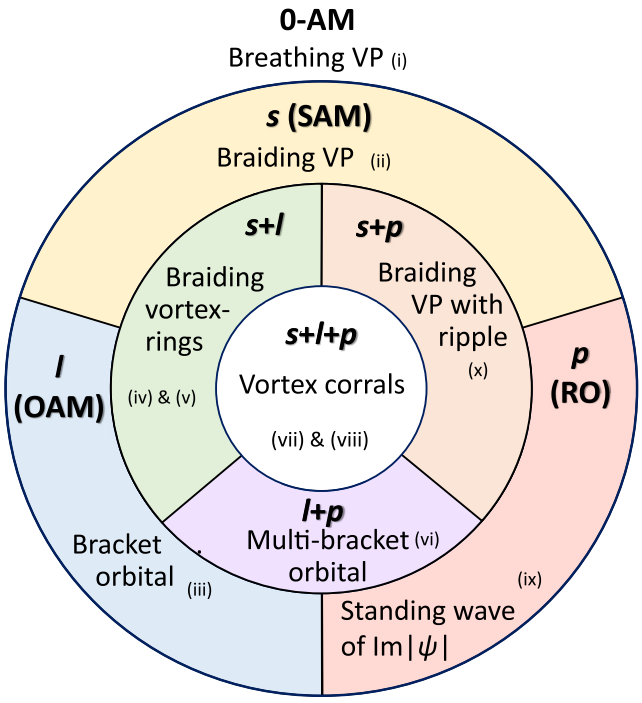



FIG. 8. Schematics QN diagram of SC states induced by LG beam. The diagram illustrates the sets and subsets of quantum numbers $s$, $l$, and $p$ for SAM, OAM, and RO. The details are shown in Table II.

TABLE II. Details of the QN diagram shown in Fig. 8. Blue and yellow dots represent the vortices with different vorticity. Black dots represent clusters of vortices or vortex droplets. Red dashed curve indicate the rotational direction. Green and purple curves in (ix) depict the curve of $\theta_s = 0$ and Im[$\psi$], respectively. Since some of the vortex motions are too complicated or there are no clear vortices, we use pink lines to represent orbitals for those situations.

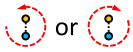
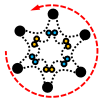
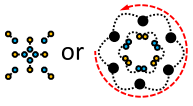
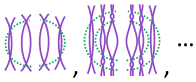
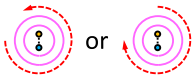
| No. | Schematic | Description |
|---|---|---|
| (i) |  | No AM: $(s, l, p) = (0, 0, 0)$. The LP Gaussian light beam has no angular momentum. The VP(s) exhibit linear or breathinglike motion, moving perpendicular to the polarization direction (see Video S1 in the Supplemental Material [26]). |
| (ii) |   | ±SAM: $(s, l, p) = (\pm 1, 0, 0)$. Right- and left-handed CP Gaussian light beams are determined by $s = -1$ and $+1$, respectively. Braiding VP(s) or braiding droplets rotate clockwise or counterclockwise around the center of the spot (see Videos S2 and S3 in the Supplemental Material [26]). |
| (iii) |   | OAM: $(s, l, p) = (0, > 0, 0)$. The LP LG light beam revolves in the right-handed direction. The dynamics of $\lvert\psi\rvert$ shows $C_2$ symmetry, and vortices move along the orbitals that have shape of round brackets when $l \geqslant 3$ (see Video S1 in the Supplemental Material [26]). |
| (iv) |  | OAM + SAM: $(s, l, p) = (-1, > 0, 0)$. These LG light beams generate a $2\lvert l - s\rvert$-fold symmetric vortex ring in the $\lvert\psi\rvert$ profile, and $\lvert l - s\rvert$-fold symmetries in both $\theta_s$ and $\omega_{v,s}$. The beams produce a star-shaped $\theta_s$, which rotates in the right-handed direction (see Video S2 in the Supplemental Material [26]). |
| (v) |   | OAM−SAM: $(s, l, p) = (1, > 0, 0)$. Similar to (iv), but produce a flower-shaped phase $\theta_s$. For $s = l = 1$, the magnetic field becomes rotationally symmetric, which results in linear motion of the vortices (see Video S3 in the Supplemental Material [26]). |
| (vi) |   | OAM and RO: $(s, l, p) = (0, > 0, > 0)$. The LP LG light beam develops nodal lines in the electric field and $z$ component of the magnetic field. For $l \geqslant 3$, these $B_z$ result in multiple regions of suppressed $\lvert\psi\rvert$, which have shapes of round brackets, in which the vortices move. For $l < 3$, these $B_z$ result in other types of orbitals along which the vortices move (see Videos S4 and S7 in the Supplemental Material [26]). |
| (vii) |  | OAM + SAM and RO: $(s, l, p) = (-1, > 0, > 0)$. This LG light beam forms coaxial multivortex rings with $\lvert l - s\rvert$-fold symmetries in both $\theta_s$ and $\omega_{v,s}$, and $2\lvert l - s\rvert$-fold symmetry in $\lvert\psi\rvert$. It generates complex vortex clusters, or so-called vortex corrals, accompanied by star-shaped set of branch cuts in $\theta_s$ that rotate in the right-handed direction. According to our tests, for $p = 1$ and 2, the results of simulations display single and double vortex rings, sometimes influenced by boundary interactions or accompanied by inter-ring dynamics (see Videos S5 and S8 in the Supplemental Material [26]). |
| (viii) |   | OAM − SAM and RO: $(s, l, p) = (1, > 0, > 0)$. Similar to (vii), but with flower-shaped set of branch cuts in $\theta_s$. For $s = l = 1$, it results in linear motion of the vortices. For $p = 1, 2$, the dynamics become increasingly intricate, with inter-ring interactions and large gradients of the phase in the vicinity of zero-$\lvert\psi\rvert$ curves (see Videos S6 and S9 in the Supplemental Material [26]). |
| (ix) |   | RO: $(s, l, p) = (0, 0, > 0)$. The LG light beam exhibits binary phase polarization. The order parameter initially presents standing waves in the imaginary component of $\psi$, accompanied by ripples in $\lvert\psi\rvert$ before vortex formation. Once the vortices emerge, the dynamics of $\lvert\psi\rvert$ exhibits linear motion of the vortices in the VPs (see Videos S4 and S7 in the Supplemental Material [26]). |
| (x) |   | ±SAM and RO: $(s, l, p) = (\pm 1, 0, > 0)$. Braiding VP(s) or braiding droplets of vortices rotate right-handedly ($s = -1$) or left-handedly ($s = +1$) around the center of the beam, accompanied by ripple patterns in $\lvert\psi\rvert$ (see Videos S5, S6, S8, and S9 in the Supplemental Material [26]). |

TABLE III. The list of $E_0$ in the units of $A_0 \cdot \omega_{GL}$.

| $p$ | | 0 | | | 1 | | | 2 | |
|---|---|---|---|---|---|---|---|---|---|
| $l$ \ $s$ | −1 | 0 | 1 | −1 | 0 | 1 | −1 | 0 | 1 |
| 0 | 2.0 | 2.0 | 2.0 | 2.0 | 2.0 | 2.0 | 3.0 | 2.0 | 3.0 |
| 1 | 2.5 | 3.0 | 4.0 | 4.0 | 3.0 | 4.0 | 5.0 | 4.0 | 6.0 |
| 2 | 6.0 | 5.0 | 3.0 | 3.5 | 4.0 | 3.5 | 5.0 | 5.0 | 4.0 |
| 3 | 8.0 | 5.0 | 5.0 | 3.5 | 3.5 | 3.5 | 5.0 | 4.0 | 4.0 |
| 4 | 8.0 | 6.0 | 6.0 | 8.0 | 5.0 | 4.0 | 8.0 | 5.0 | 4.0 |
| 5 | 8.0 | 7.0 | 7.0 | 8.0 | 6.0 | 6.0 | 8.0 | 8.0 | 8.0 |

### 2. *Vortex corral imprinted by LG beams with $p > 0$ and angular momentum*

When considering $p$ with AMs, the situation becomes more complex. The magnitude of $B_z$ in the inner and outer rings differs significantly. Since formation of vortices strongly depends on the value of the local magnetic flux, the vortices in the outer rings might start appearing when the order parameter in the inner ring is fully suppressed. We do not investigate a full range of amplitudes of the electric field to study all the possible dynamics in the outer and inner rings, and consider here only values of the amplitude of $\boldsymbol{E}$ similar to the ones used in the $p = 0$ case. The complete set of results for QNs in the range $s = -1 \sim 1$, $l = 0 \sim 5$, and $p = 0 \sim 2$, along with simulations from 0 to $120\tau_{GL}$, are available in Videos S1–S9 in the Supplemental Material [26]. Details of the simulations can also be found in Appendix B.

Even with strict constraints on the amplitude of $\boldsymbol{E}$, the QN of $p$ still introduces new phenomena in the simulations. It leads not only to the appearance of the multiple orbitals of vortices, but to the interactions between orbitals, and results in a lot of kinds of vortex clusters. In particular, structured light with nonzero $p$ values generates a larger hollow-ring structure, but still inducing supercurrents and vortices at the center in some cases. This effect resembles an optically induced quantum mirage of superconducting order parameters, similar to the quantum corral effect [38]. Consequently, we refer to these vortex clusters as vortex corrals. To illustrate these findings, we have selected several noteworthy cases for discussion, which are demonstrated in Fig. 7.

*Multiorbital structure.* First, the QN $p$ is directly linked to the formation of multiorbital structures. In Fig. 7(a), a typical multiorbital structure is shown, where the inner and outer orbitals share the same symmetry, both exhibiting convex branch cuts. This example also clearly illustrates the chain of vortex droplets. Across various QN configurations, this phenomenon occurs more readily when $(s, l, p) = (1, \geqslant 2, 2)$, resulting in a multi-flower-shaped phase, as demonstrated in Fig. 19 and in Video S9 in the Supplemental Material [26].

In the absence of SAM, for QNs $l > 1$, $s = 0$, and $p = 0$, for which the results are shown in Sec. III A 4, the pure OAM effect leads to stable, bracketlike structures when $l \geqslant 3$. However, when combined with the RO, $p$, the results become more complex, sometimes producing exotic patterns such as a digital "8" profile for $(s, l, p) = (0, 2, 2)$ and "X" profile for $(s, l, p) = (0, 1, 2)$. In most cases, especially for

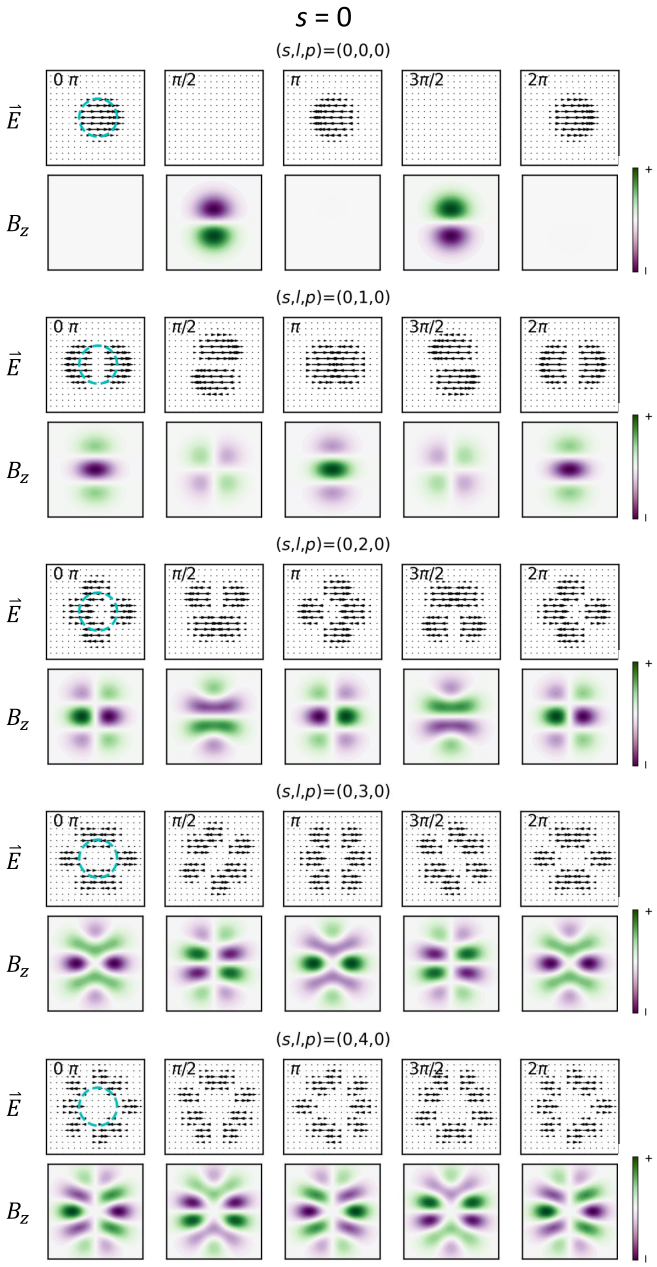



FIG. 9. Snapshots of normalized $E$ and normalized $B_z$ at $\omega_{EM}t = 0, \pi/2, \pi, 3\pi/2, 2\pi$ for each of the light sources labeled $(s = 0, l, p)$. The dashed blue circles mark the spot size.

TABLE IV. The list of $L$ in the units of $\xi$.

| $p$ | | 0 | | | 1 | | | 2 | |
|---|---|---|---|---|---|---|---|---|---|
| $l$ \ $s$ | −1 | 0 | 1 | −1 | 0 | 1 | −1 | 0 | 1 |
| 0 | 25 | 25 | 25 | 30 | 30 | 30 | 40 | 40 | 40 |
| 1 | 25 | 25 | 25 | 30 | 30 | 30 | 40 | 40 | 40 |
| 2 | 25 | 25 | 25 | 30 | 30 | 30 | 40 | 40 | 40 |
| 3 | 25 | 25 | 25 | 30 | 30 | 30 | 40 | 40 | 40 |
| 4 | 30 | 25 | 25 | 40 | 30 | 30 | 40 | 40 | 40 |
| 5 | 30 | 25 | 25 | 40 | 30 | 30 | 40 | 40 | 40 |

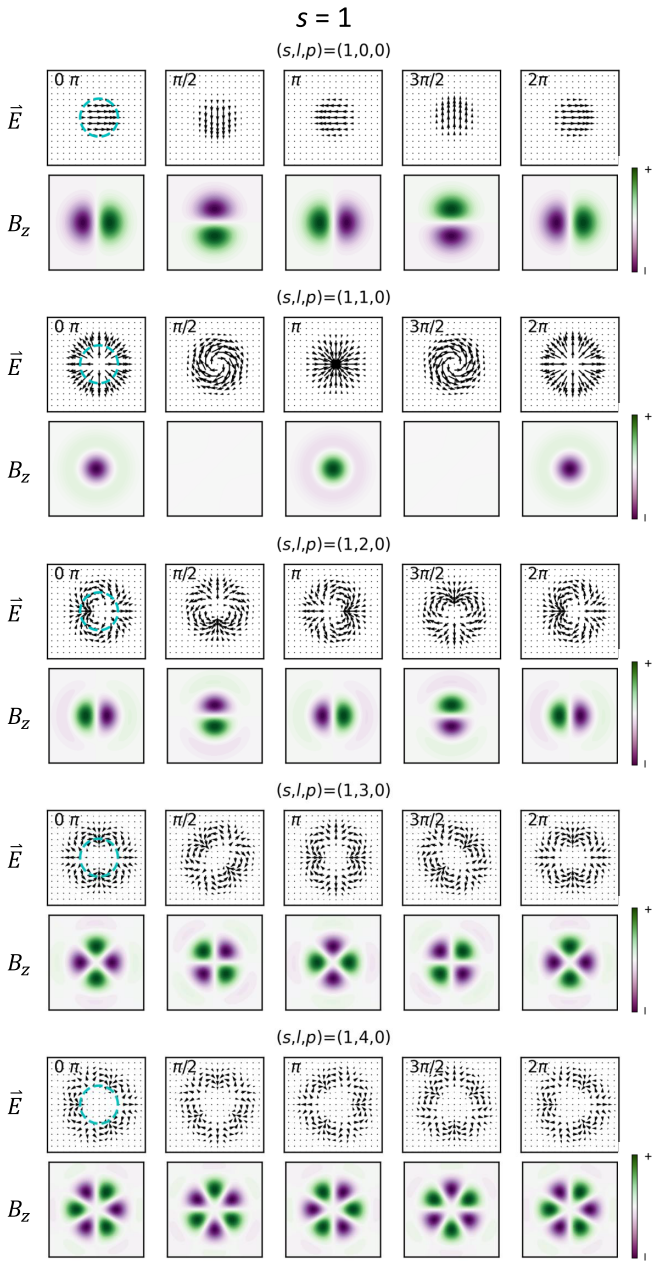



FIG. 10. Snapshots of normalized $E$ and normalized $B_z$ at $\omega_{\mathrm{EM}}t = 0, \pi/2, \pi, 3\pi/2, 2\pi$ for each of the light sources labeled $(s = 1, l, p)$. The dashed blue circles mark the spot size.

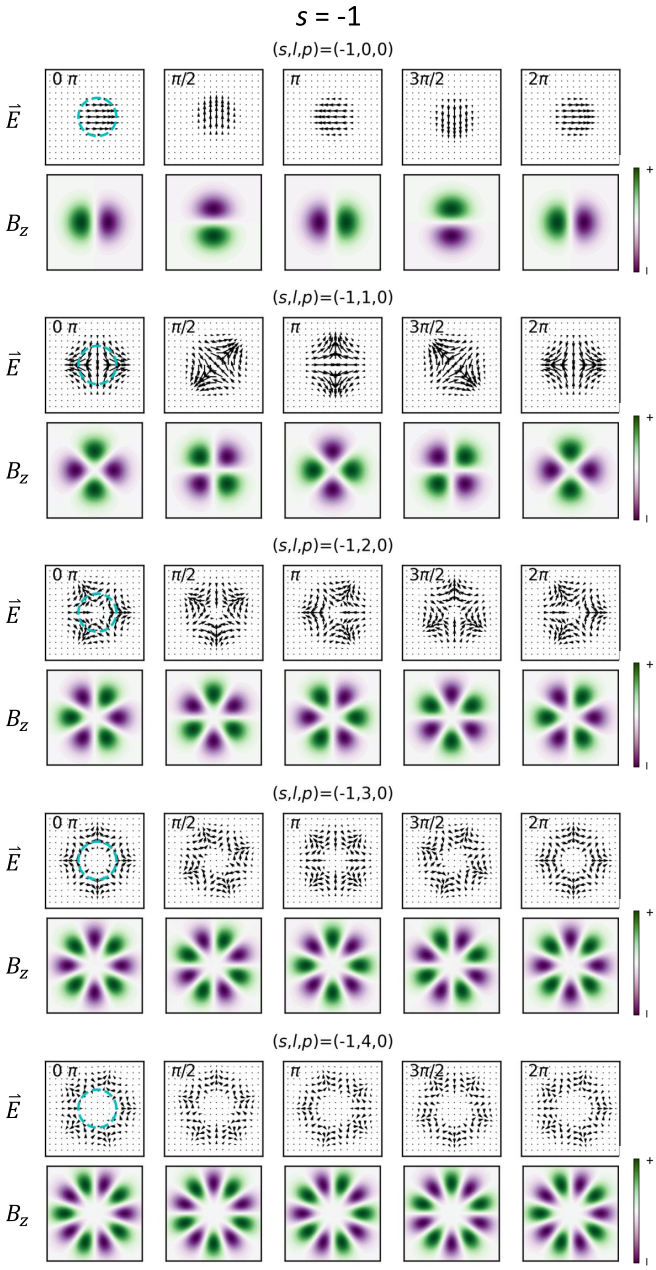



FIG. 11. Snapshots of normalized $E$ and normalized $B_z$ at $\omega_{\mathrm{EM}}t = 0, \pi/2, \pi, 3\pi/2, 2\pi$ for each of the light sources labeled $(s = -1, l, p)$. The dashed blue circles mark the spot size.

$l \geqslant 3$, the structures form multilayered bracket patterns oriented perpendicularly to each other. These outcomes are presented in Fig. 19 and Videos S1, S4, and S5 in the Supplemental Material [26].

*Curvy voids* In the case shown in Fig. 7(b), curvy voids (regions of suppressed amplitude of the order parameter) appear in the $|\psi|$ profile. In the phase profile, there is a distinguishable contour of circular shape that corresponds to these voids. It is formed by a fast change in the phase gradient. The data suggest that across certain segments of this contour, the amplitude of the gradient is very large, or there might be a discontinuity in the phase value. If such a discontinuity exists, its origin remains unclear and needs further investigation. The contour also contains four singularity points around which the phase winds by $2\pi$, which points to the presence of vortices in the voids. This contour remains stable and rotates with the light. This phenomenon is also frequently observed when $(s, l, p) = (1, \geqslant 1, 2)$, exhibiting a multi-flower-shaped phase, as demonstrated in Fig. 19 and Videos S6 and S9 in the Supplemental Material [26].

*Nonrotating vortex corral.* With higher RO, $p$, and $|l - s| = 0$, the motion of vortices occurring in the radial direction resembles the case $|l - s| = 0$ for $p = 0$ described in Sec. III A 3. In this case, the profile of magnetic field does not rotate, which results in a linear motion of the vortices in the VPs. The resulting configuration of VPs resembles a corral

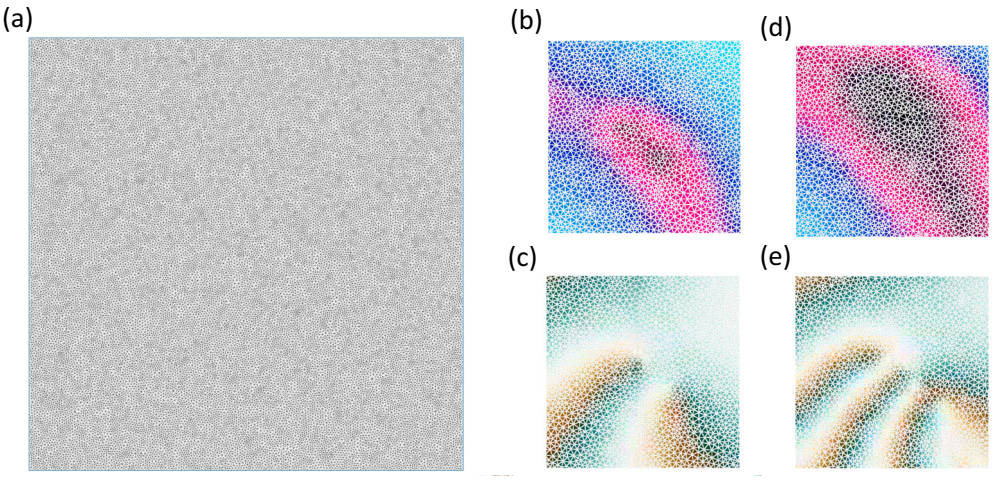



FIG. 12. (a) The mesh grid for the square film with a side length of $L = 25\xi$ shown as black lines. The mesh grids (white lines) are overlaid with $|\psi|$ in (b) and (d) and with $\theta_s$ in (c) and (e) for demonstration. The order parameter snapshots are taken from Fig. 5(c). Figures (b) and (c) correspond to the vortex case ($E_0 = E_1$ in Fig. 5(c)), while (d) and (e) show the droplet case ($E_0 = E_3$ in Fig. 5(c)).

structure, which we call a VP corral. The example in Fig. 7(c) also shows that the VP generation occurs in the vicinity of the first and third nodal lines of $B_z$, but not in the vicinity of the second nodal line of $B_z$. Similar dynamics of vortices occurs for the light beams $LG_{11,1}$ and $LG_{21,1}$, as demonstrated in Videos S6 and S9 in the Supplemental Material [26].

*Abnormal motion of the outer vortex ring.* For $p = 2$, the outer ring is close to the boundary. When $s = -1$, it shows

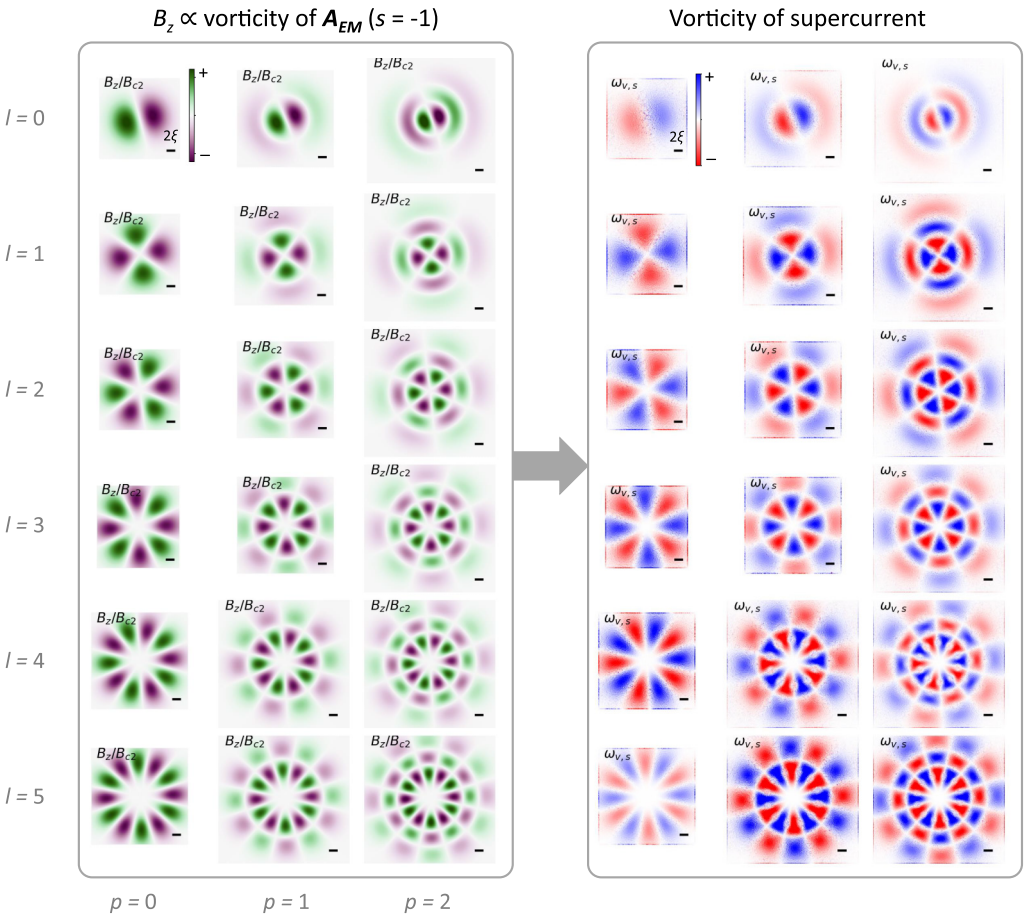



FIG. 13. The vorticity of vector potential and imprinted vorticity of supercurrent before vortex generation. The light sources are $LG_{pl,-1}$. All of profiles are snapshots at $20\tau_{GL}$.

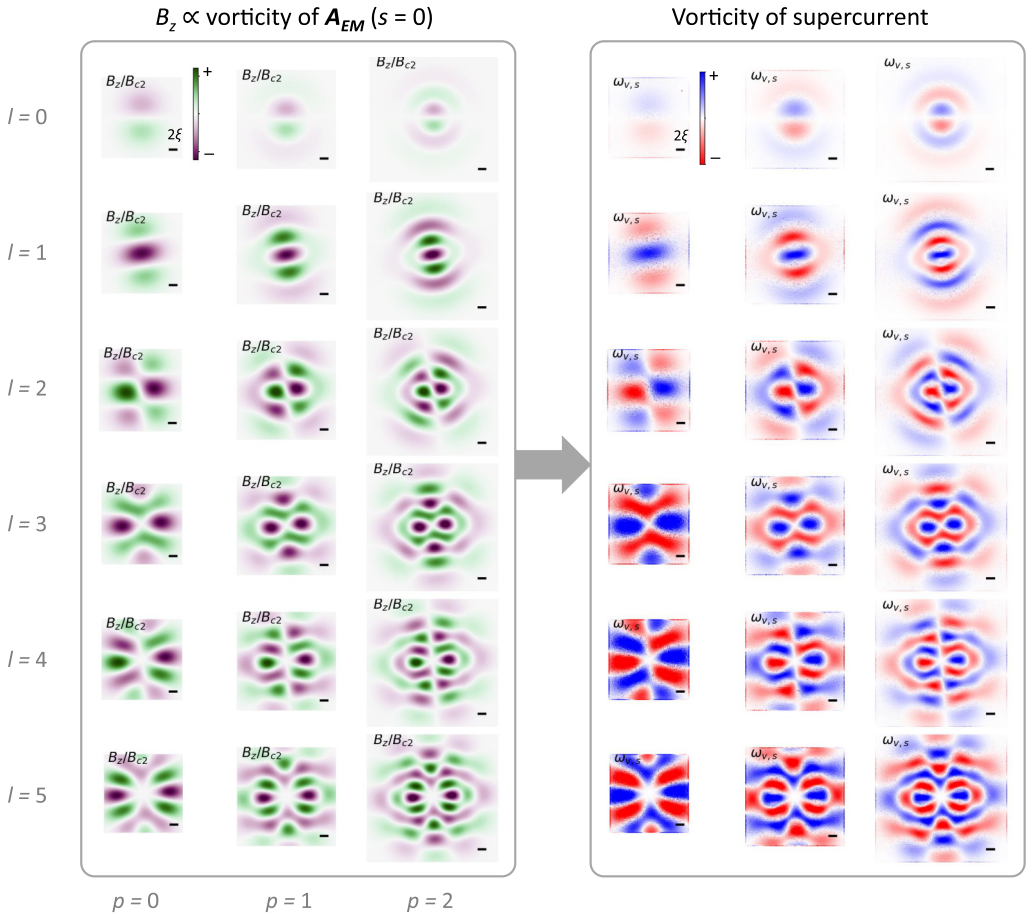



FIG. 14. The vorticity of vector potential and imprinted vorticity of supercurrent before vortex generation. The light sources are $\mathrm{LG}_{\mathrm{pl},0}$. All of profiles are snapshots at $20\tau_{\mathrm{GL}}$.

the abnormal motion of the outer vortex ring, unlike in the case of $s = 1$ and other vortex rings when $p = 0, 1$. The VPs are generated on diagonals of the sample, which for $l = 2$ does not respect the symmetry of $B_z$. Besides, those VPs are trapped at the same locations, recombining shortly after the generation, at least for the period of time investigated in the simulation. This can be attributed to the closeness of the outer ring to the boundary. This phenomenon can also be observed in other cases, such as when $(s, l, p) = (-1, \geqslant 2, 2)$, though it is less pronounced compared to the $\mathrm{LG}_{21,-1}$ case.

*Interorbital interaction of vortices.* The previous cases exhibit various multiorbital behaviors, but there is no direct connection between the orbitals. However, with higher values of $p$ and $l$, and a sufficient applied electric field amplitude, the orbitals can become interconnected, forming a vortex cluster similar to a snowflake. Figure 7(e) shows a typical example of a "vortex flake" induced by $\mathrm{LG}_{14,-1}$. In this case, aside from the vortices aligned with the rotational direction, there are also VPs oriented transversely along the ring. This structure allows for the coexistence of both rotating and linear vortex motions.

### C. Diagram of SC states dependent on $s$, $l$, and $p$

Considering the QNs $s$, $l$, and $p$, the QN diagram can be represented as a collection of QN sets and their union of subsets, as illustrated in Fig. 8. From this QN diagram, the order parameter dynamics induced by structured light can be categorized into the subsets mentioned in Table II (with $l > 0$ as an example, where the sign of SAM determines whether the rotation aligns with or opposes the OAM). Besides, the snapshots and dynamical simulation results are provided in Appendix F and Videos S1–S9 in the Supplemental Material [26].

## IV. CONCLUSION

In this work, we demonstrate the *quantum printing* of structured light on superconductors, where the vorticity of the gauge potential of light is imprinted to the vorticity of the SC supercurrent and vortex motion. By tuning the QNs of LG beams—including SAM, OAM, and RO—and adjusting the amplitude of the electric field, we can steer and manipulate superconducting vortices.

We demonstrated a variety of vortex dynamics, including breathing VPs [e.g., Fig. 3(a)], braiding VPs [e.g., Fig. 3(b)], vortex droplets [e.g., Figs. 5(c) and 5(d)], optical angular momentum-induced linear VPs' motion [e.g., Fig. 16(d)], and swirling vortex rings with star- and flower-shaped phase profiles [e.g., Figs. 3(d) and 3(g)]. We also observe more complex phenomena of vortex corrals such as vortex-flake structures [e.g., Fig. 7(e)], multiringed vortex configurations [e.g., Figs. 7(a) and 7(b)], standing wave patterns (e.g., Fig. 6),

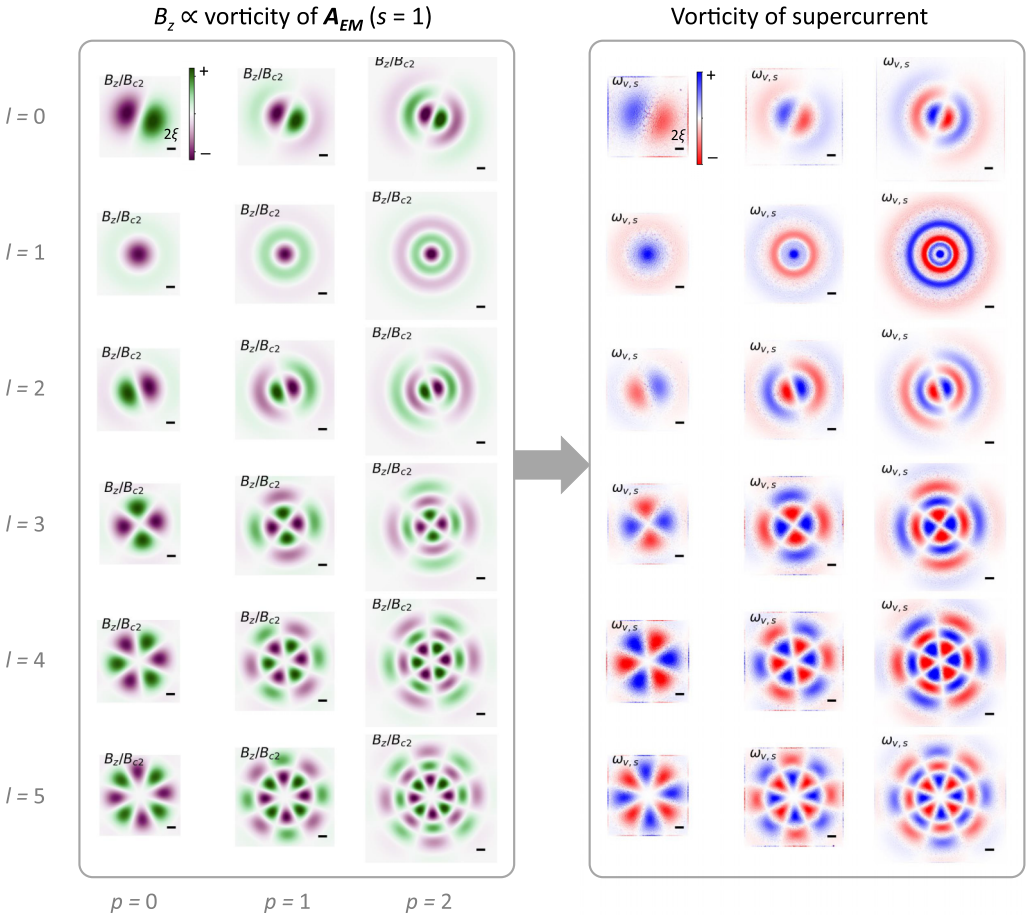



FIG. 15. The vorticity of vector potential and imprinted vorticity of supercurrent before vortex generation. The light sources are $LG_{pl,1}$. All of profiles are snapshots at $20\tau_{GL}$.

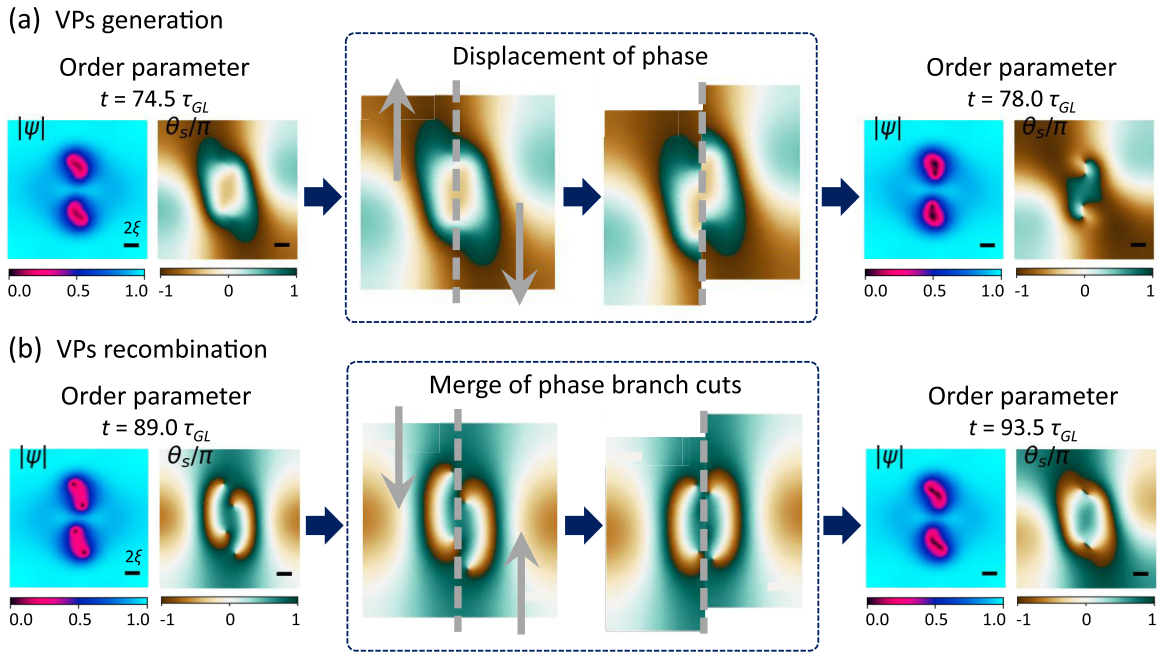



FIG. 16. Demonstrations of the effects related to displacing of the phase induced by $LG_{01,0}$. (a) The VPs' generation due to displacing of the phase. The left and right panels capture the moments just before and after the VP formation, respectively, while the middle panel presents a schematic of the process. (b) The VP recombination driven by the restoration of phase branch cuts. The left and right panels show snapshots of the VP recombination, with the middle panel illustrates how the displacement gradually returns to its original state.

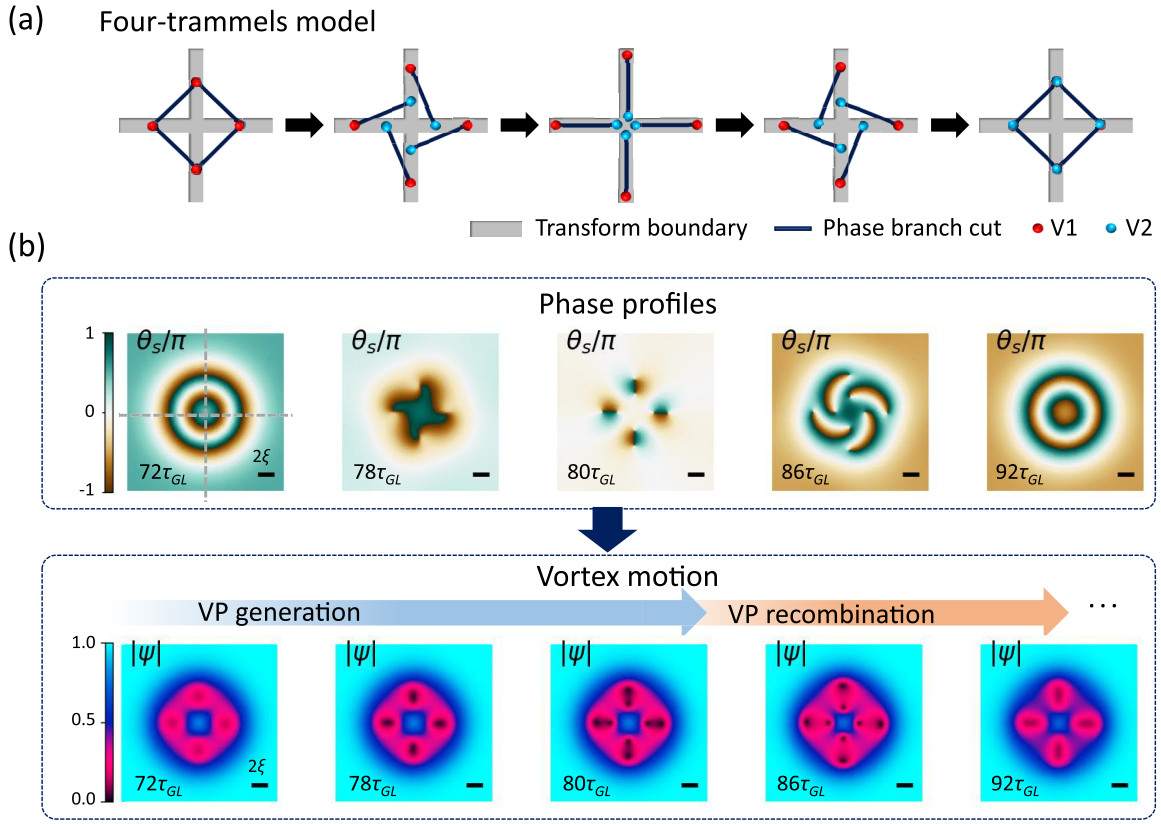



FIG. 17. The trammel model induced by $LG_{01,1}$. (a) Toy model of four trammels moving along transform boundaries. The lines of the boundary are shown as gray areas, and the black sticks represent the trammels in the toy model and correspond to the phase branch cuts in SC phase. The blue and red balls represent the ends of the trammels and also correspond SC vortices with different vorticities. When the blue and red balls overlap, it signifies the annihilation of a vortex and an antivortex. (b) Snapshots of $\theta_s$ associated with the trammel model, along with the corresponding profile of $|\psi|$, illustrating the vortices.

and asymmetric orbital behavior [e.g., Fig. 4(a)]. These phenomena reflect the direct imprint of light's QNs onto the SC system, effectively imprinting the structured light's symmetry and dynamics to the superconducting condensate.

Through simulations, we show how manipulating the QNs of the light beam allows for sophisticated control over vortex formation and motion, which offers potential applications in fields like quantum hydrodynamics and optical manipulation of SC states. The experimentally observable signatures of the phenomena we present here have been discussed in previous work [20]. We note that the experimental observation of this rich set of vortex dynamics will require coupling structured THz light to a superconducting thin film while taking steps to avoid undesired heating and quasiparticle excitation of the film (Appendix G). More specific examples of detection would depend on the experimental platform used to detect vortex motion. We mention the $I(V)$ characteristics, local scanning tunneling microscope (STM) probes, and perhaps angle-resolved photoemission spectroscopy in the time domain as possible routes to probe the predicted effects.

The diagram of QNs in Fig. 8 summarizes the collective response of the SC order parameter to different combinations of QNs carried by light. It demonstrates how structured light serves as an optical "stamp," being able to imprint its symmetry onto the superconductor and influence vortex dynamics. The results pave the way for further exploration of light-superconductor interactions, with potential implications for controlling topological defects, vortex sheet [39,40], optical quantum switches, SC devices [18,41], and other phenomena in condensed matter systems.

## ACKNOWLEDGMENTS

Part of this work was carried out while A.B. and his collaborators were visiting the Department of Physics of Stanford University and SLAC National Accelerator Laboratory. We are grateful to T. Devereaux and members of his group for discussions and hospitality during our visit. We also acknowledge useful discussions with E. Babaev, S. Bonetti, K. Bondarenko, A. Chainani, B. Friedman, G. Jotzu, J. T. Heath, H. Hwang, R. B. Laughlin, D. H. Lee, W. Lee, M. Manson, A. Metha, A. Pathapati, Z. X. Shen, Y. Suzuki, C. L. C. Triola, O. Tjernberg, V. Unikandanunni, J. Weissenrieder, P. Wong, and M. Verma. This work was supported by the US DOE BES DE-SC0025580 (A.B. and T.Y.) and the European Research Council under the European Union Seventh Framework ERC-2018-SYG 810451 HERO (H.Y.). GitHub of lg-tdgl: This work is based on the pytdgl developed by Logan Bishop-Van Horn. The development for structured light dynamics was supported by US DOE Office of Basic Energy Sciences under Award No. DE-SC-0025580. The documentation for pytdgl can be found at [42].

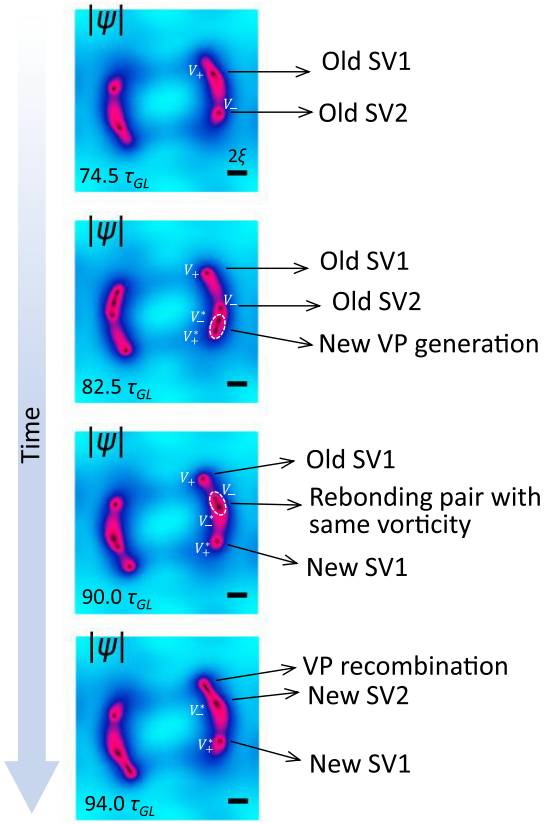



FIG. 18. The time evolution of the bond-debond-rebond process of VPs with light $LG_{04,0}$. The snapshots at different times represent the four different processes. When $t = 74.5\tau_{GL}$: Old single vortex (SV) residue from the last cycle. When $t = 82.5\tau_{GL}$: VP generation starts to debond and rebond with the adjacent SV that has the same vorticity. When $t = 90.0\tau_{GL}$: The rebonding pair move stably and rotate along the orbital. When $t = 94.0\tau_{GL}$: The rebonding pair bump into the old SV at the end point, and one of the vortices in VP recombines with the old SV.

## DATA AVAILABILITY

The data that support the findings of this article are openly available [25]; embargo periods may apply.

## APPENDIX A: CONTRIBUTION OF $r$ AND $\varphi$ TO $B_z$

For the LG beam, the $z$ component of the magnetic field, $B_z = (\nabla \times \boldsymbol{A})_z$, can be nonzero. The amplitude of the electric field in Eq. (3) consists of three components,

$$u_{p,l}(r, \varphi, z) = u_0 u_r u_\varphi, \tag{A1}$$

where $u_0$, $u_r$, and $u_\varphi$ are the constant of amplitude equal to $E_0$, radial distribution of amplitude, and azimuthal distribution, respectively. When the light sources with constant $u_\varphi$, such as $LG_{p0,s}$ for any $s, p$, the curl of transverse mode becomes the curl of amplitude distribution as $\nabla \times (u_0 u_r u_\varphi \hat{\boldsymbol{E}}_{\rm pol}) = u_0 u_\varphi \nabla \times (u_r \hat{\boldsymbol{E}}_{\rm pol})$, where $\hat{\boldsymbol{E}}_{\rm pol} = \cos\varphi_{xy}\hat{\mathbf{e}}_x + e^{-i\sigma}\sin\varphi_{xy}\hat{\mathbf{e}}_y$ represents the unit vector for polarization based on Eq. (4). Hence, it is completely dominated by the distribution of intensity. If we consider the OAM with the azimuthal term $\exp il\varphi$ where the azimuthal angle can be expressed as $\varphi = \arctan(y/x)$, then the derivative of $\varphi$ becomes non-negligible. The results of numerical calculations are provided in Figs. 9–11.

## APPENDIX B: SIMULATION INPUTS: $E$, $L$, AND MESH

In this Appendix, we provide information on the amplitude of the electric field $E_0$ in Eq. (3) (see Table III), the sample size $L$ (see Table IV), and the mesh we used in the simulations.

The conditions of LG beam are chosen to demonstrate the dynamics of long-lived VPs. Based on the simulation results in Fig. 6 of our previous manuscript [20], we select a light frequency of $\omega_{\rm EM} = \omega_{\rm GL}/40$, which supports sustained vortex motion without immediate annihilation. The chosen values of $E_0$ are sufficient to trigger vortex generation and, in some cases, result in the creation of multiple VPs to meet the threshold for nucleation. For instance, as discussed in Sec. III A3, the minimum number of generated VPs is 2 for $(s, l, p) = (0, 1, 0)$ and 4 for $(1, 1, 0)$.

It is important to note that the peak intensity of the structured light is not solely determined by $E_0$, but also by the spatial structure of the beam due to three main factors: (1) The peak intensity of LG beams is not solely determined by $E_0$. For example, OAM-carrying beams, which have hollow centers, exhibit lower peak amplitudes compared to Gaussian beams with the same $E_0$. (2) The resulting $B_z$ field, derived from the curl of the vector potential, depends on the specific structure of the light. (3) The geometry of the sample and the symmetry of the resulting $B_z$ may influence the minimum threshold for a VP generation. Table III lists the $E_0$ values used in all simulations unless otherwise specified in the figure captions.

In addition, the quantum numbers of the light affect the beam profile and effective size—even for a fixed spot size $w_0$—which also influences the choice of sample size $L$. This selection is for a trade-off between minimizing computational cost and avoiding artificial boundary effects.

Therefore, to provide sufficient intensity for vortex generation without fully destroying the superconducting state, we present vortex dynamics using different combinations of $E_0$ and $L$, depending on the beam's quantum numbers.

The step size of the mesh should be smaller than the unit of length, $\xi$, in order to resolve the vortices. Even if the morphology of vortex is not the topic of this work, however, the scale of the size remains important because sometimes the vortices are too crowded and therefore merge to vortex droplets. The step size needs to be sufficiently small to support this result. Here, we demonstrate the mesh for the case $L = 25\xi$ in Fig. 12(a). We also overlap the meshgrid with the vortices and the vortex droplet from the snapshots in Fig. 5(c). Apparently, in the case of the droplet [Fig. 12(e)], which represents vortices close to each other, the meshgrid still can spatially resolve the singularity points of $\theta_s$. In real physical units, these parameters are determined by factors such as temperature and material properties. Fixing the temperature at $0.99T_c$, and following the analysis in our previous work [20], $E_0$ and $L$ are expected to be kV/cm–MV/cm and micrometers, respectively.

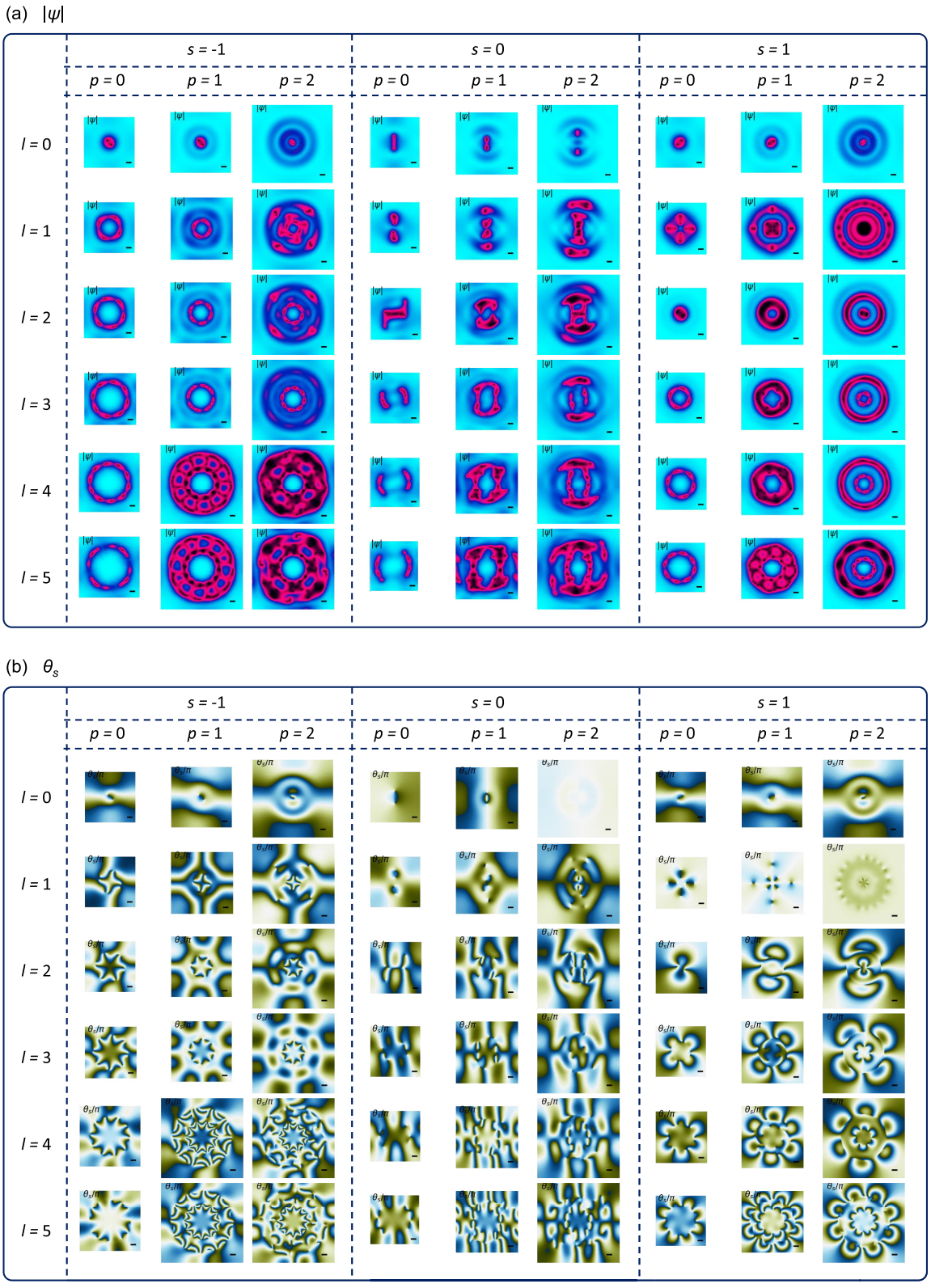



FIG. 19. The snapshots of (a) $|\psi|$ and (b) $\theta_s$ at $100\tau_{\mathrm{GL}}$.

## APPENDIX C: IMPRINT EFFECT OF VORTICITY

In Sec. III A 1, the vorticity of the vector potential, also equivalent to $B_z$, can directly imprint to the vorticity of the supercurrent. The numerical results of imprinting profiles are demonstrated in this Appendix in Figs. 13–15.

## APPENDIX D: SIMILARITIES BETWEEN THE TRAMMEL MODEL AND THE CASE OF $LG_{01,1}$

We discussed the dynamics of phase branch cuts, highlighting their mechanistic similarities to trammels for the case of $LG_{01,1}$ light. In this Appendix, we demonstrate in more detail the dynamics of branch cuts induced by light sources $LG_{01,0}$ and $LG_{01,1}$.

For $LG_{01,0}$, Fig. 16 exhibits two key moments: the generation of VPs at $t = 74.5$–$78.0\tau_{GL}$ in panel (a) and the recombination of VPs at $t = 89.0$–$93.5\tau_{GL}$ in panel (b). These processes resemble shear movement along $x = 0$, where two VPs are generated and recombined at the end points of the branch cuts.

Figure 17 illustrates the similarity between the trammel model and the dynamics of the phase branch cuts induced by $LG_{01,1}$. The trammel of Archimedes, a type of ellipsograph [43], demonstrates a mechanism for converting a linear motion into a circular one. In the simulation with $LG_{01,1}$, the rotational motion of the phase branch cuts resembles the action of four trammel sticks as shown in Fig. 17, while the linear motion of the VPs corresponds to the motion of the end points of these sticks. Recombination and generation of the VPs occur when the stick end points overlap and detach, respectively. This model effectively illustrates the underlying mechanism by which SAM and OAM are transferred to produce the linear motion of vortices.

## APPENDIX E: FORMATION OF REBONDING VPS WITH OAM-CARRYING LIGHT SOURCES

In Sec. IIIA4(d), we mentioned that the bond-debond-rebond process of VPs can be observed in the case of bracket-shaped orbitals. The time evolution of the process is shown in Fig. 18. It demonstrates an observable rebonding VP of vortices with the same vorticity and residual vortices (marked SV in Fig. 18) at the end points of the orbital. It illustrates both the bond-debond-rebond process of VPs and the generation and recombination processes between a residual vortex and a vortex in the rebonding VP. This sophisticated dynamics can be observed in the cases of $s = 0$ and $l \geqslant 3$ in Video S1 in the Supplemental Material [26].

## APPENDIX F: SNAPSHOT OF ORDER PARAMETERS

In this Appendix, we demonstrate spatial dependence of the order parameter. The results of simulations for $|\psi|$ and $\theta_s$ for all light sources are shown in Figs. 19(a) and 19(b), respectively.

## APPENDIX G: EXPERIMENTAL CONSIDERATION OF LG BEAM

In this Appendix, we extend the discussion from the Gaussian beam mentioned in the previous work [20] (Secs. IV A and IV B) to the LG beam. According to the desription of LG beam as Eq. (3), which depicts the intensity function $u_{p,l}$, we incorporate the normalization constant $C_{pl}$ to ensure that the total intensity distribution satisfies the condition

$$\int_0^{2\pi} d\theta \int_0^{\infty} dr \cdot r \left|\frac{E_{EM}}{E_0}\right|^2 = \int_0^{2\pi} \int_0^{\infty} dr \cdot r \left|\frac{u_{p,l}}{E_0}\right|^2 = 1. \tag{G1}$$

In our simulations, the field amplitude $E_0$ directly influences vortex generation, and the heating effect scales accordingly with the power estimated from the integral of $|E_{EM}|^2$.

While we did not explore the minimum value of $E_0$ needed for generation of VPs for different types of LG beams, it remains on the same order (or at most, one order larger, as mentioned in Table III) as for the linearly polarized Gaussian beam considered above. Consequently, the heat deposited from the LG beams with different sets of quantum numbers will be comparable to the calculation in Sec. IV B of the previous manuscript [20].


[1] Y. Zhao and H. Xu, Laser-induced thermocapillary flows on a flowing soap film, Phys. Rev. Fluids **9**, L022001 (2024).

[2] X. Zhu, C. Vannahme, E. Højlund-Nielsen, N. A. Mortensen, and A. Kristensen, Plasmonic colour laser printing, Nat. Nanotechnol. **11**, 325 (2016).

[3] Y. Zhang, Y. Jiao, C. Li, C. Chen, J. Li, Y. Hu, D. Wu, and J. Chu, Bioinspired micro/nanostructured surfaces prepared by femtosecond laser direct writing for multi-functional applications, Int. J. Extreme Manuf. **2**, 032002 (2020).

[4] X. Zhu, W. Yan, U. Levy, N. A. Mortensen, and A. Kristensen, Resonant laser printing of structural colors on high-index dielectric metasurfaces, Sci. Adv. **3**, e1602487 (2017).

[5] D. Böcherer, R. Montazeri, Y. Li, S. Tisato, L. Hambitzer, and D. Helmer, Decolorization of lignin for high-resolution 3D printing of high lignin-content composites, Adv. Sci. **11**, 2406311 (2024).

[6] B. Garai, A. Mallick, and R. Banerjee, Photochromic metal–organic frameworks for inkless and erasable printing, Chem. Sci. **7**, 2195 (2016).

[7] M. Regehly, Y. Garmshausen, M. Reuter, N. F. König, E. Israel, D. P. Kelly, C.-Y. Chou, K. Koch, B. Asfari, and S. Hecht, Xolography for linear volumetric 3D printing, Nature (London) **588**, 620 (2020).

[8] D. Loterie, P. Delrot, and C. Moser, High-resolution tomographic volumetric additive manufacturing, Nat. Commun. **11**, 852 (2020).

[9] R. Zhao, L. Huang, and Y. Wang, Recent advances in multi-dimensional metasurfaces holographic technologies, PhotoniX **1**, 20 (2020).

[10] M. Basini, M. Pancaldi, B. Wehinger, M. Udina, T. Tadano, M. Hoffmann, A. Balatsky, and S. Bonetti, Terahertz electric-field driven dynamical multiferroicity in $SrTiO_3$, Nature (London) **628**, 534 (2024).

[11] C. Davies, F. Fennema, A. Tsukamoto, I. Razdolski, A. Kimel, and A. Kirilyuk, Phononic switching of magnetization by the ultrafast Barnett effect, Nature (London) **628**, 540 (2024).

[12] J. Luo, T. Lin, J. Zhang, X. Chen, E. R. Blackert, R. Xu, B. I. Yakobson, and H. Zhu, Large effective magnetic fields

from chiral phonons in rare-earth halides, Science **382**, 698 (2023).
[13] H. Fujita and M. Sato, Encoding orbital angular momentum of light in magnets, Phys. Rev. B **96**, 060407 (2017).
[14] C. D. Parmee, M. R. Dennis, and J. Ruostekoski, Optical excitations of skyrmions, knotted solitons, and defects in atoms, Commun. Phys. **5**, 54 (2022).
[15] T. Mizushima and M. Sato, Imprinting spiral Higgs waves onto superconductors with vortex beams, Phys. Rev. Res. **5**, L042004 (2023).
[16] I. Gnusov, S. Harrison, S. Alyatkin, K. Sitnik, J. Töpfer, H. Sigurdsson, and P. Lagoudakis, Quantum vortex formation in the "rotating bucket" experiment with polariton condensates, Sci. Adv. **9**, eadd1299 (2023).
[17] L. Dominici, A. Rahmani, D. Colas, D. Ballarini, M. De Giorgi, G. Gigli, D. Sanvitto, F. P. Laussy, and N. Voronova, Coupled quantum vortex kinematics and Berry curvature in real space, Commun. Phys. **6**, 197 (2023).
[18] H. Yerzhakov, T.-T. Yeh, and A. Balatsky, Induction of orbital currents and Kapitza stabilization in superconducting circuits with Laguerre-Gaussian microwave beams, Phys. Rev. B **110**, 144519 (2024).
[19] Y. Fang, J. Kuttruff, D. Nabben, and P. Baum, Structured electrons with chiral mass and charge, Science **385**, 183 (2024).
[20] T.-T. Yeh, H. Yerzhakov, L. B.-V. Horn, S. Raghu, and A. Balatsky, preceding paper, Quantum printing and induced vorticity in superconductors I: Linearly polarized light, Phys. Rev. Res. **7**, 043111 (2025).
[21] DeepAI, 3D Objects Generator (September 2024 version), https://deepai.org/machine-learning-model/text2img.
[22] L. Kramer and R. J. Watts-Tobin, Theory of dissipative current-carrying states in superconducting filaments, Phys. Rev. Lett. **40**, 1041 (1978).
[23] R. J. Watts-Tobin, Y. Krahenbuhl, and L. Kramer, Nonequilibrium theory of dirty, current-carrying superconductors: Phase-slip oscillators in narrow filaments near $T_c$, J. Low Temp. Phys. **42**, 459 (1981).
[24] L. Bishop-Van Horn, PyTDGL: Time-dependent Ginzburg-Landau in Python, Comput. Phys. Commun. **291**, 108799 (2023).
[25] GitHub repository link of LG-TDGL: https://github.com/TienTienYeh/lg-tdgl.
[26] See Supplemental Material at http://link.aps.org/supplemental/10.1103/dqv7-w2w4 for instructions of simulation codes and videos.
[27] A. Forbes, M. De Oliveira, and M. R. Dennis, Structured light, Nat. Photon. **15**, 253 (2021).
[28] J. Wang, J. Liu, S. Li, Y. Zhao, J. Du, and L. Zhu, Orbital angular momentum and beyond in free-space optical communications, Nanophotonics **11**, 645 (2022).
[29] X. Gu, M. Krenn, M. Erhard, and A. Zeilinger, Gouy phase radial mode sorter for light: Concepts and experiments, Phys. Rev. Lett. **120**, 103601 (2018).
[30] J. Pearl, Current distribution in superconducting films carrying quantized fluxoids, Appl. Phys. Lett. **5**, 65 (1964).
[31] C. Kittel and P. McEuen, *Introduction to Solid State Physics* (John Wiley & Sons, Hoboken, New Jersey, 2018).
[32] T. R. Lemberger, I. Hetel, J. W. Knepper, and F. Yang, Penetration depth study of very thin superconducting Nb films, Phys. Rev. B **76**, 094515 (2007).
[33] J. Draskovic, T. R. Lemberger, B. Peters, F. Yang, J. Ku, A. Bezryadin, and S. Wang, Measuring the superconducting coherence length in thin films using a two-coil experiment, Phys. Rev. B **88**, 134516 (2013).
[34] T. Yokoyama, Creation of superconducting vortices by angular momentum of light, J. Phys. Soc. Jpn. **89**, 103703 (2020).
[35] V. Plastovets, I. Tokman, B. Lounis, A. Mel'nikov, and A. Buzdin, All-optical generation of Abrikosov vortices by the inverse Faraday effect, Phys. Rev. B **106**, 174504 (2022).
[36] N. B. Kopnin, *Theory of Nonequilibrium Superconductivity* (Oxford University Press, 2001), Vol. 110.
[37] A. Bencheikh, M. Fromager, and K. A. Ameur, Generation of Laguerre–Gaussian $LG_{p0}$ beams using binary phase diffractive optical elements, Appl. Opt. **53**, 4761 (2014).
[38] M. Crommie, C. Lutz, D. Eigler, and E. Heller, Quantum corrals, Physica D **83**, 98 (1995).
[39] G. E. Volovik, Superfluids in rotation: Landau–Lifshitz vortex sheets vs Onsager–Feynman vortices, Phys. Usp. **58**, 897 (2015).
[40] E. Thuneberg, Introduction to the vortex sheet of superfluid $^3$He-A, Phys. B: Condens. Matter **210**, 287 (1995).
[41] V. V. Dremov, S. Y. Grebenchuk, A. G. Shishkin, D. S. Baranov, R. A. Hovhannisyan, O. V. Skryabina, N. Lebedev, I. A. Golovchanskiy, V. I. Chichkov, C. Brun *et al.*, Local Josephson vortex generation and manipulation with a magnetic force microscope, Nat. Commun. **10**, 4009 (2019).
[42] pyTDGL: Time-dependent Ginzburg Landau in Python, https://py-tdgl.readthedocs.io/en/latest/.
[43] J. Downs, *Practical Conic sections: The Geometric Properties of Ellipses, Parabolas and Hyperbolas* (Courier Corporation, Garden City, New York, 2003).